Journal Pre-proof

A detailed kinetic model for the reduction of oxygen on LSCF-GDC composite cathodes

Alessandro Donazzi, Giulio Cordaro, Andrea Baricci, Zhao-Bin Ding, Matteo Maestri

PII: S0013-4686(20)30011-6

DOI: https://doi.org/10.1016/j.electacta.2020.135620

Reference: EA 135620

To appear in: *Electrochimica Acta*

Received Date: 23 June 2019

Revised Date: 1 January 2020

Accepted Date: 2 January 2020

Please cite this article as: A. Donazzi, G. Cordaro, A. Baricci, Z.-B. Ding, M. Maestri, A detailed kinetic model for the reduction of oxygen on LSCF-GDC composite cathodes, *Electrochimica Acta* (2020), doi: https://doi.org/10.1016/j.electacta.2020.135620.

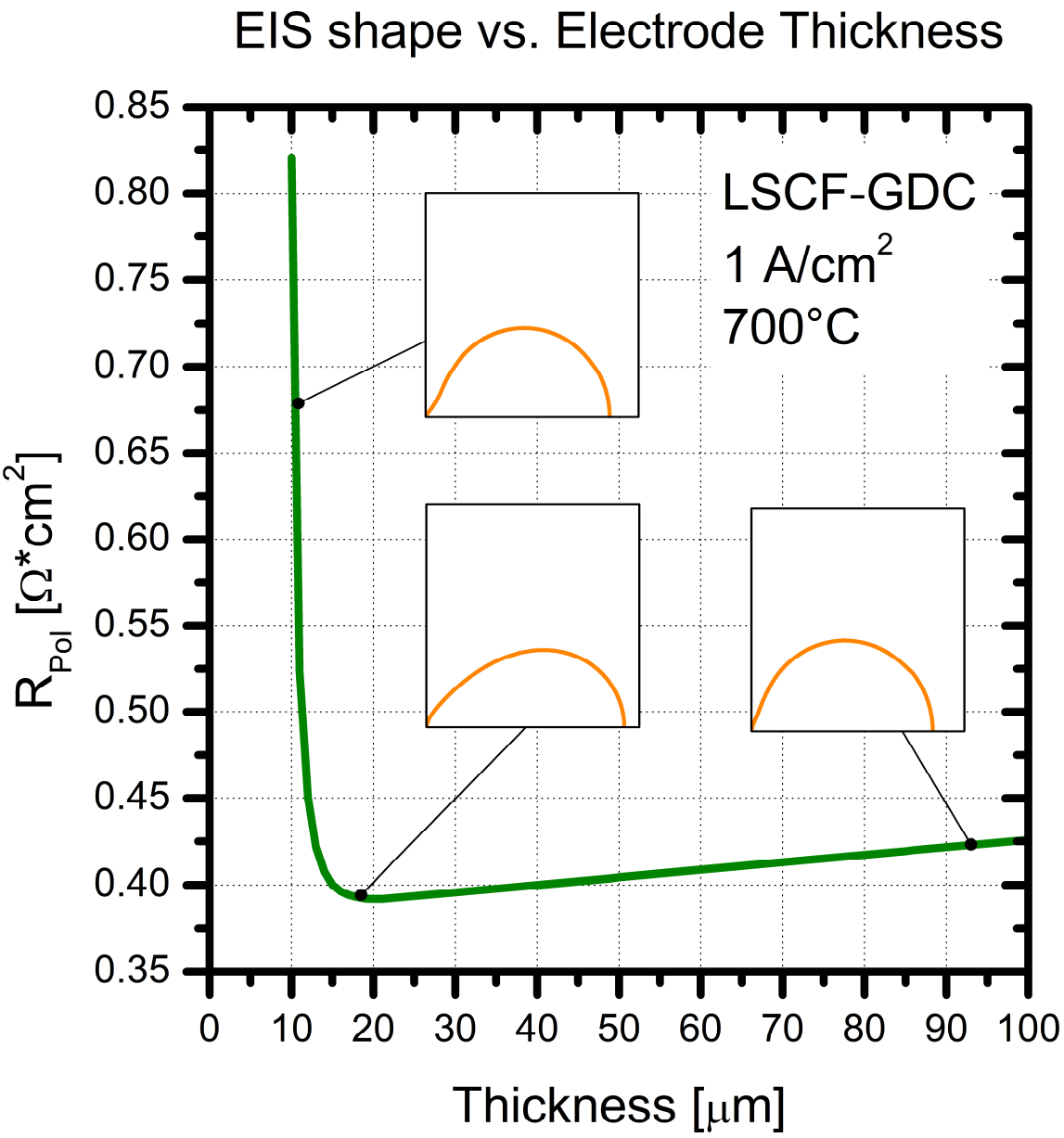
EIS shape vs. Electrode Thickness
LSCF-GDC
1 A/cm2
700°C
R_Pol [Ω*cm2]
Thickness [μm]
0.85
0.80
0.75
0.70
0.65
0.60
0.55
0.50
0.45
0.40
0.35
0
10
20
30
40
50
60
70
80
90
100

A detailed kinetic model for the reduction of oxygen on LSCF-GDC composite cathodes

Alessandro Donazzi[*], *Giulio Cordaro, Andrea Baricci, Zhao-Bin Ding, Matteo Maestri*

Dipartimento di Energia, Politecnico di Milano,

Via Lambruschini 4, 20156 Milano, Italy

*corresponding author:

Alessandro Donazzi

Dipartimento di Energia

Via Lambruschini 4, 20156 Milano (Italy)

Phone: 0039 02 2399 8651

Fax: 0039 02 2399 8566

e-mail: alessandro.donazzi@polimi.it

Abstract

A kinetic investigation of the Oxygen Reduction Reaction (ORR) is performed on LSCF-GDC composite cathodes ($La_{0.4}Sr_{0.6}Co_{0.2}Fe_{0.8}O_{3-\delta}/Ce_{0.9}Gd_{0.1}O_{2-\delta}$ 50/50) spanning a wide range of operating conditions. EIS tests are carried out on symmetric cells between 700°C and 560°C at OCV, with O_2/N_2 mixtures at varying O_2 molar fraction (5-21%). A dynamic, one-dimensional, physic model of the LSCF-GDC electrode is applied to rationalize the experimental results. The model simulates the spectra by solving mass and charge conservation equations, including terms for gas diffusion in the porous electrode and solid state transport in both the LSCF and the GDC lattice. A thermodynamically consistent, detailed kinetic scheme is applied to describe the ORR mechanism, which takes into account elementary steps of adsorption and desorption, first and second electronation at the gas/electrode interface, interfacial and lattice ion transfer. A full set of rate parameters (pre-exponential factors and activation energies) is derived by fitting to inhouse-measured impedance data, and validated against a well-established literature dataset. The sensitivity analysis supports the prevailing role of the TPB route over the 2PB route, and highlights that the transfer of a single-charged oxygen adatom from the LSCF surface to the GDC lattice governs the ORR. The model clarifies the origin of distortions in measured impedance arcs, and captures the effect of O_2 pressure on the observed electrochemical activity.

Keywords: LSCF, GDC, EIS, ORR, microkinetics

1. Introduction

LSCF-GDC composites are state-of-the-art cathodes for applications based on Intermediate Temperature Solid Oxide Fuel Cells (IT-SOFC). LSCF ($La_{0.4}Sr_{0.6}Co_{0.2}Fe_{0.8}O_{3-\delta}$) is a perovskite with mixed ionic and electronic conductive (MIEC) properties, which confer this material the capability of supplying electrons to adsorbed oxygen and transfer oxide ions within the lattice structure. Such multifunctional character allows to break the paradigm of an oxygen reduction reaction (ORR) mechanism exclusively based on the Three Phase Boundary (TPB) concept, and opens up an additional transport route, which requires only two active interfaces (2PB), since oxygen is activated and transferred within the same phase [1-3]. Although LSCF is often used as a pure material, composite architectures in combination with GDC ($Ce_{0.9}Gd_{0.1}O_{2-\delta}$) are preferential in applications, in order to boost the electrolyte/electrode contact area and limit the thermal expansion mismatch.

Given the wide application of LSCF-GDC composites, the quantitative understanding of the ORR is a requisite for the optimization, under a design viewpoint (choice of LSCF/GDC ratio, electrode thickness and particle size), as well as under an operational viewpoint (minimization of degradation processes, maximization of the performance). Several model approaches have been adopted to describe the ORR mechanism, which are typically based on impedance spectroscopy analyses [4-18]. The majority of the studies follows the equivalent circuit method [3, 5-8, 11, 13, 15, 18]. Apart of fully phenomenological descriptions based on RC and CPE elements, the introduction of Gerischer elements provides more reliable physical meaning: nonetheless, extrapolation of the results is difficult and mechanistic elucidation is limited. A second approach entails the application of physical models, wherein fundamental equations of charge, mass and energy conservation are solved [10, 16, 19-27]. Depending on the assumptions and on the dimensionality of the problem,

several parameters can be accounted for in terms of microstructure, operative conditions, kinetics and thermodynamics. On the one hand, the practicality of these models decreases, due to the considerable number of pieces of information required and to the increasing complexity of the numerical procedures; on the other hand, the descriptive capability grows and a larger pool of experimental data can be included in the analysis.

The ALS model [28, 29] and the transmission line model [30] are fundamental and milestone examples of physical approaches. Main assumptions of these approaches are the individuation of a rate determining step, usually taken as a first order surface exchange rate, as well as the consideration of single-phase electrodes. An extension of the ALS model to composite electrodes is presented by Mortensen et al. [31, 32] and validated against impedance spectra measured on symmetric cells mounting LSF-GDC electrodes. A macro-homogeneous approach is adopted and the composite electrode is described as a continuum, which groups the MIEC phase and the GDC phase in one single ion-conductive phase. The mass conservation equation considers the transport of vacancies according to a diffusion coefficient which averages those of GDC and LSF based on porosity and tortuosity parameters. Thermodynamic rigor is guaranteed by the derivation of the Nernst-Plank equation starting from the chemical potential and by the adoption of thermodynamic factors: noteworthy, the driving chemical potential is defined for an electronated pseudo-species (a double electronated vacancy), which allows to obtain explicit relationships. Based on a similar approach, Nielsen et al. [6] derive lumped equations (Finite Length Gerischer equations, FLG) for the impedance of composite cathodes based on a MIEC phase and show that the balance among vacancy diffusion coefficient, surface exchange rate and electrode's length governs the impedance measurements, which can turn from Gerischer-like into different shapes. The authors analyze three data sets

collected on LSCF-GDC cathodes, in terms of equivalent circuits: depending on the microstructure and on electrode's performance, either the FLG element or the traditional Gerischer element is considered in series with a Warburg element able to describe the contribution of gas diffusion impedance.

A common result of the previous models is that the surface kinetic constant plays a key role in establishing the shape and amplitude of the spectra. Detailed kinetic models overcome the simplification of a single first order step and potentially capture conditions where lumped models break down, such as when the RDS changes or when a competition between 2PB and TPB routes occurs. Yurkiv et al. [10] present a composite electrode model with a detailed multistep kinetic scheme, which is able to reconcile EIS experiments on symmetric cells with LSCF-GDC cathodes, in air and under open cell conditions, between 775 K and 1075 K. The scheme is thermodynamically consistent thanks to the definition of enthalpy and entropy formation parameters, some of which are derived by fitting the simulated spectra to the data points. Also in this case, the composite electrode is described as a continuum: one charge conservation equation is written and no explicit ion diffusion treatment is included. In contrast, Laurencin and coworkers [14, 33] rigorously apply individual charge and mass conservation balances to both the MIEC and the electrolyte phase. These authors validate a four-step kinetic scheme based on single-phase LSCF electrode experiments spanning over a wide range of cathodic and anodic bias. The model is further extended to predict polarization and impedance experiments collected on LSCF-GDC composites. A set of kinetic parameters is derived by fitting to the spectra, under the assumptions of negligible surface potential and invariance of the oxygen adsorbates surface coverage with respect to temperature. An accurate insight in the transition between kinetic regimes is provided, which neatly outlines that the electrode microstructure and the applied voltage are crucial in establishing whether

the bulk or the surface reduction pathway prevails. With reference to LSM-YSZ composites, Banerjee and Deutschmann [27] follow an intermediate approach, wherein the two phases are treated separately, being LSM exclusively an electronic conductor. The resulting framework mirrors that of distributed-charge composite cells models [34, 35]. A detailed and thermodynamically consistent mechanism is proposed, and several sets of impedance experiments taken from relevant literature are reconciled. The key-role of surface diffusion of oxygen adsorbates emerges as a distinguishing point of LSM-based electrode models. Along with this result, Bertei et al. [23] discuss the consequences of moving from the 2PB to the TPB pathway by application of a physical model of LSM-YSZ composites, and show that the bias overpotential determines the transition. These four detailed models share some important features. The surface charge-transfer rates include a surface potential, first proposed by Fleig [36, 37] and Liu [38-40], whose nature is related to the specific capability of MIEC materials to create an additional capacitive interface between charged oxygen adsorbates and positive electronic countercharges [36], other than the electrode/electrolyte capacitive interface. In Refs. [10] and [27], the charge-transfer rates are expressed directly as a function of the phases' potentials, according to the framework by Bessler [41], rather than following the Butler-Vomer approach, which requires fixing one or more reference potentials and which is instead adopted in Refs. [14] and [23].

In this work, a physically-based electrode model with a multistep detailed kinetic scheme is developed and applied to rationalize inhouse impedance spectroscopy experiments performed on composite LSCF-GDC cathodes, covering a wide range of operating conditions in terms of temperature (560°C to 700°C) and O_2 fraction (5% to 21% v/v). The model includes the individual description of the MIEC phase and of the GDC phase with solid state diffusion parameters, as well as

dedicated balances for intermediate surface species. Thermodynamic consistency principles are applied to the reaction steps, starting from literature estimations of formation parameters of surface and lattice species. A Butler-Volmer framework is chosen to describe the elementary charge-transfer steps, setting appropriate equilibrium potentials. A full set of rate parameters (pre-exponential factors and activation energies) is extracted by fitting to the impedance data, and further validated against the well-defined experiments by Nielsen et al. [6] (moderate coarse structure dataset), also outside the original calibration range (up to 800°C). A sensitivity analysis (SA) is also carried out to highlight the rate determining step, which shows the predominance of the TPB over the 2PB reduction pathway. Overall, the model serves as a basis for the optimization of the structural properties of applicative LSCF-GDC composite cathodes.

2. Experimental

Symmetric cells were prepared using GDC electrolytes and LSCF-GDC cathodes. GDC powders ($Gd_{0.10}Ce_{0.90}O_{1.95}$, GDC10, FuelcellMaterials) were die-pressed at 5 ton/cm^2 for 3 minutes and sintered in air at 1400°C for 12 h (2°C/min heating and cooling ramp). The resulting pellets (1.1 cm diameter and 1 mm thickness) reached 96% theoretical density, as verified with buoyancy balance measurements in ethanol. A commercial LSCF-GDC composite ink (FuelcellMaterials) was applied to prepare the cathode. The ink consisted of a mixture of 50 wt% $La_{0.6}Sr_{0.4}Co_{0.2}Fe_{0.8}O_{3-\delta}$ and 50 wt% GDC10 suspended in α-terpineol, for a total loading of solid particles of ~70%. The electrode layers were deposited on the pellet surface by blade coating a slurry, obtained by addition of isopropyl alcohol (0.1 g/g ink) and graphite (0.12 g/g ink) to the precursor ink. After application, each layer

underwent a drying step at 150°C for 5 h. Adhesion of the layers on the GDC pellet was achieved by calcination in air at 1000°C for 2 h (1°C/min heating/cooling ramp). The thickness of the layers, their adhesion to the pellet and the morphology of the sintered particles were assessed with Scanning Electron Microscopy (SEM) using a Carl Zeiss EVO50VP instrument equipped with an Energy Dispersive Spectrometer (EDS) for elemental analysis. An average thickness of 70 μm was measured for the cathode layers (Fig. 1a and Table 1). Based on this value, starting from the measured weight of each electrode, 40% porosity was determined. This porosity value was verified via mercury porosimetry (Micromeritics AuotoPore IV), which allowed also to evaluate the pore size (0.3 μm). The morphology of the sintered particles (Fig. 1b) revealed homogenous, with no appreciable difference between LSCF and GDC, which showed an average diameter of ~1 μm. Though, given the difficulty in establishing this value, the particle size distribution of the LSCF-GDC composite was also determined on the ink powders by means of laser granulometry (Cilas 1180). Prior to the analyses, the samples (~20 mg samples) were exposed to ultrasonic stirring in isopropyl alcohol for 10 minutes, in order to dissolve the ink and break the agglomerates. The results of the granulometric analyses (Fig. 1c) revealed a broad distribution with the presence of a main peak centered at 0.8 μm, followed by a shoulder at 8 μm. Considering the thickness of the layers, this second peak could be reasonably attributed to residual undissolved agglomerates.

The EIS measurements were carried out in a Probostat unit (Norwegian Electro Ceramics) equipped with a potentiostat/galvanostat (AMEL 7050) and a frequency response analyzer (FRA). The experiments were performed between 560°C and 700°C, at Open Circuit Voltage (OCV), with 10 mV voltage amplitude and 10 mHz to 10 kHz frequency range. The temperature was ramped up to 700°C and decreased 50°C stepwise. At each temperature level, the impedance spectra were

collected at three O_2 partial pressures, 21%, 10% and 5% v/v, with N_2 to balance. After varying the concentration of O_2, stable measurements were obtained usually within 45 to 60 minutes. The experiments at 21% and 5% O_2 were also repeated using He instead of N_2 as the diluent, in order to verify the impact of mass transfer limitations. In all the experiments, 50 Ncc/min gas flow rate was supplied to each side of the cell. Before the admission to the oven, the gas mixtures were dehydrated passing through a moisture trap (Sigma Aldrich). The current collectors were fabricated by applying a silver mesh with silver paint to each electrode of the cell. Three LSCF-GDC/GDC/LSCF-GDC symmetric cells were tested and the resulting spectra were averaged. The experimental variance among the results amounted to ~8% with respect to both the real part and the imaginary part of the spectra.

3. Electrode model

A one dimensional, dynamic and heterogeneous model is developed to simulate the impedance spectra measured on LSCF-GDC cathodes. The model relies on the following assumptions:

1. The electrode is isothermal and isobaric, and the gas behaves ideally.
2. A *continuum-level* description is adopted for each phase of the composite electrode. GDC and LSCF are treated as distinct and continuous solids, which reciprocally contact at the interface.
3. The electrode structure is a random binary mixture of percolated particles, whose effective properties are evaluated starting from bulk material properties, reduced by the introduction of appropriate factors. The morphologic, transport and structural parameters are constant in the electrode volume (isotropic parameters).

4. The current collectors are zero-dimensional perfect electronic conductors.
5. The LSCF phase is a non-ideal dilute solution. The non-ideality is taken into account by introduction of the thermodynamic factor A, which is considered independent of the vacancy concentration and exclusively dependent on temperature. The concentration of background positive charges, which consists of Sr, La and Fe ions, is constant and homogenous in the whole electrode volume. The same assumption is proposed in the ALS model [28] and later by Jin et al. [42] for pure LSCF electrodes, wherein the inert and immobile ions are treated as a unique solvent.
6. The GDC phase is equilibrated and homogeneous under all the explored conditions. Consequently, the amount of vacancies and oxide ions is constant, gradient-less and fixed to the equilibrium value. This assumption translates the fact that the concentration of vacancies in GDC is negligibly perturbed by the transfer that stems from the neighboring LSCF phase.
7. GDC is considered as a non-adsorptive purely ionic conductor, with transference number equal to 1. O_2 adsorption and activation occurs exclusively on the LSCF surface and no electrons are provided to the intermediate species either via the GDC lattice or via the GDC surface. The dense GDC electrolyte of the cell is also considered an electrical insulator and no electronic leakage current is accounted for.
8. LSCF is a MIEC phase, able to conduct ions and electrons. Within the composite electrode volume, the electronic current is exclusively transferred through the LSCF phase, while the ionic current is simultaneously transferred through GDC and through the LSCF phase.

9. Electron-hole pairs are equilibrated. This assumption is also proposed in the ALS model [28]. It leads to the adoption of a single Fermi level for both these species (Section 3.5).

Figure 2a displays a representation of the model domain, with definition of the flux directions, coordinates and boundaries. The domain includes only the composite electrode volume. The interface between the current collector (CC) and the electrode is located at the entrance, and it is set as z = 0. The electrode/electrolyte interface is located at the exit of the domain, and it is set as z = End, which corresponds to the electrode thickness L. It is intended that the gas is admitted to the cathode passing through a recirculation chamber, which is located upstream the current collector and which is treated as a Continuously Stirred Tank Reactor (CSTR) [34, 35, 43]. The volume V_{CSTR} of the recirculation chamber is 2.5 cm^3. Figure 2b displays a detail of the interface between the composite cathode and the electrolyte. The composite electrode is approximated as a continuous series of GDC particles, extending from the electrolyte into the electrode, which contact LSCF along their axis. The representation of the contacting particles is provided in panel C, wherein the adsorption surface, the contact surface and the TPB line are highlighted. A single intersection is accounted for between each particle of LSCF and GDC, with a 15° contact angle [44-46].

3.1 Kinetic mechanism

The ORR is described according to a five-step kinetic mechanism. The LSCF phase is indicated with the subscript M (MIEC), while the GDC phase with the subscript E (electrolyte). Molecular oxygen O_2 is adsorbed on the LSCF surface by dissociation on two free sites $ (step S1), with formation of two adsorbed oxygen atoms (O adatoms in the following).

$$O_2 + 2\$ \leftrightarrow 2O_M^{ads} \qquad \text{(S1)}$$

The electronation process is split in two individual steps. Each O adatom is first electronated to produce a single charged adsorbed oxygen atom O_M^{-ads} (S2). This charged oxygen atom acquires the second electron and reacts with a vacancy in the LSCF lattice, producing an oxide ion $O_{o,M}^{x}$ and a free surface site \$ (S3).

$$O_M^{ads} + e^- \leftrightarrow O_M^{-ads} \qquad \text{(S2)}$$

$$O_M^{-ads} + V_{\ddot{o},M} + e^- \leftrightarrow O_{o,M}^{x} + \$ \qquad \text{(S3)}$$

The oxide ion is finally transferred across the LSCF/GDC interface by reaction with a vacancy in the GDC lattice (S4). Steps 3 and 4 describe the so-called two phase boundary (2PB) pathway, since the ion transfer reaction exclusively requires crossing the contact surface between the MIEC and the electrolyte phase. The surface step S3 is coupled with the ionic transference step S4 via vacancy diffusion in the LSCF lattice.

$$O_{o,M}^{x} + V_{\ddot{o},E} \leftrightarrow O_{o,E}^{x} + V_{\ddot{o},M} \qquad \text{(S4)}$$

The competing three phase boundary mechanism (TPB) is also accounted for, by inclusion of an additional step (S5), wherein the single charged oxygen atom reacts with a vacancy of the GDC lattice, producing an oxide ion in the electrolyte.

$$O_M^{-ads} + V_{\ddot{o},E} + e^- \leftrightarrow O_{o,E}^{x} + \$ \qquad \text{(S5)}$$

Similar sets of reactions are proposed in the literature. The main differences concern the adoption of holes or electrons as active species, and the description of the electronation process. On LSM-YSZ cathodes, Zhang et al. [38] propose the same ORR mechanism, considering diffusion of charged oxygen toward the TPB. Still with reference to LSM-YSZ cathodes, Banerjee and Deutschmann [27] compare a series of

alternative mechanisms, introducing holes: the authors discuss different routes for the surface electronation process, coming to the conclusion that the most comprehensive mechanism includes the presence of a super-oxo O_2^- species, which decomposes into two charged oxygen atoms. In the case of LSCF-GDC composite cathodes, Laurencin and coworkers [14] propose a mechanism based on holes, which lumps the electronation process in one single step (S2 + S3). Yurkiv et al. [10], instead, split the electronation in two reactions, but consider exclusively the 2PB pathway and assume an initial step of non-dissociative O_2 adsorption. Notably, since these authors describe the composite electrode as a single-phase continuum, the second electronation reaction has the same stoichiometry of step S5, even though it is intended as the combination of the incorporation of an oxide ion in LSCF (S3) and its transfer across the LSCF/GDC interface (S4), leading to a 2PB pathway. An additional role for GDC is included, which hosts on its surface super-oxo O_2^- species. As a matter of fact, the present choice of a five-step ORR mechanism is based, on the one hand, on the larger agreement found upon the kinetics of LSCF, and on the other hand, on the reasonable economy of unknown parameters to be determined (i.e. surface diffusion coefficients). The presence of a super-oxo species is neglected based on the non-adsorptive character of GDC (assumption 7).

3.2 Model equations

The diffusion of O_2 in the porous electrode is modeled with a simple Fick-type approach (Eq. 1 and Eq. 2). The effective diffusion coefficient takes into account both molecular and Knudsen diffusivity according to the Bosanquet relationship (Eq. 3), and it is calculated considering the measured porosity ε and approximating the tortuosity τ to 1/ε.

$$\varepsilon \cdot \frac{dC_{O_2}}{dt} = -\frac{dJ_{O_2}}{dz} - a_v^{ads} \cdot r_1 \quad (1)$$

$$J_{O_2} = -D_{O_2}^{eff} \cdot \frac{dC_{O_2}}{dz} \quad (2)$$

$$\frac{1}{D_{O_2}^{eff}} = \frac{1}{D_{O_2,N_2}^{Mol,eff}} + \frac{1}{D_{O_2}^{Knu,eff}} \quad (3)$$

The net rate of adsorption r_1 (Section 3.4) is referred to the LSCF surface a_v^{ads}, which is calculated according to the percolation theory [47]. On this surface, mass balances are considered for the adsorbed intermediates, namely the oxygen adatom (Eq. 4) and the single charged oxygen species (Eq. 5). The surface concentration of these species is expressed as a function of the surface concentration of the active sites Γ and of the coverage fractions θ_i. Consistently with the mechanistic description of a competition between the 2PB and the TPB pathway, r_5 is referred to the surface contact line per unit volume λ_{TPB}. The conservation of the total number of surface sites is applied to calculate the coverage of the free sites (Eq. 6).

$$a_v^{ads} \cdot \Gamma \cdot \frac{d\theta_{O_M^{ads}}}{dt} = a_v^{ads} \cdot (2 \cdot r_1 - r_2) \quad (4)$$

$$a_v^{ads} \cdot \Gamma \cdot \frac{d\theta_{O_M^{-ads}}}{dt} = a_v^{ads} \cdot (r_2 - r_3) - \lambda_{TPB} \cdot r_5 \quad (5)$$

$$\theta_F + \theta_{O_M^{ads}} + \theta_{O_M^{-ads}} = 1 \quad (6)$$

A distinguishing feature of the model is the inclusion of two distinct conservation equations to describe the simultaneous ionic transport within the LSCF and the GDC phase. In the first case, since the lattice vacancy is a non-equilibrated key-species in the ORR mechanism, the material balance is expressed is terms of concentration $C_{V_{\ddot{o},M}}$ and molar flux density $J_{V_{\ddot{o},M}}$ (Eq. 7). The rate of second electronation r_3 is referred to the LSCF surface, while the rate of ion transport across

the LSCF/GDC interface r_4 requires the specific interfacial area a_v^{int}. f_M (Table 1) is the volume fraction of the LSCF particles in the LSCF-GDC mixture, while 1-ε is the volume fraction of the solid in the electrode.

$$(1-\varepsilon)\cdot f_M \cdot \frac{dC_{V_{\ddot{o},M}}}{dt} = -\frac{dJ_{V_{\ddot{o},M}}}{dz} - a_v^{ads}\cdot r_3 + a_v^{int}\cdot r_4 \qquad (7)$$

$$J_{V_{\ddot{o},M}} = -A\cdot D_{V_{\ddot{o},M}}^{eff}\cdot\frac{dC_{V_{\ddot{o},M}}}{dz} - \frac{z_{V_{\ddot{o}}}F\cdot D_{V_{\ddot{o},M}}^{eff}}{RT}\cdot C_{V_{\ddot{o},M}}\cdot\frac{d\phi_M^b}{dz} \qquad (8)$$

The mathematical form of the molar flux density (Eq. 8) evidences that the migration term is associated to the bulk potential ϕ_M^b of the LSCF phase, while the diffusion term to the axial gradient of vacancy concentration. The equation is derived by substituting the electrochemical potential of the vacancies (Eq. 9) into the definition of the flux density (Eq. 10), considering the Nernst-Einstein relation and a non-ideal solid solution (assumption 5). Accordingly, as demonstrated in Ref. [48], the thermodynamic factor A appears as a multiplier of the gradient of vacancy concentration, whereas the gradient of bulk potential is driven exclusively by the self-diffusion coefficient $D_{V_{\ddot{o},M}}$ owing to the definition of conductivity and of vacancy activity $\hat{a}_{V_{\ddot{o},M}}$.

$$\bar{\mu}_{V_{\ddot{o},M}} = \mu_{V_{\ddot{o},M}}^0 + RT\cdot ln\left(\hat{a}_{V_{\ddot{o},M}}\right) + z_{V_{\ddot{o}}}\cdot F\cdot\phi_M^b \qquad (9)$$

$$J_{V_{\ddot{o},M}} = -\frac{\sigma_{ion,M}^{eff}}{z_{V_{\ddot{o}}}^2\cdot F^2}\cdot\frac{d\bar{\mu}_{V_{\ddot{o},M}}}{dz} \qquad (10)$$

The concentration of oxide ions in LSCF is calculated by including the conservation of oxygen lattice sites C_{mc}, which are considered constant in the whole electrode volume as well as under all the explored temperature and pressure conditions (Eq. 11). This equation translates the fact that the total stoichiometric number of oxygen sites is

given by the sum of sites occupied by an oxide ion and empty sites. $C_{mc,M}$ is taken equal to 8.48×10^4 mol/m^3.

$$C_{mc,M} = C_{V_{\ddot{o},M}} + C_{O^x_{o,M}} \qquad (11)$$

Since the GDC phase is equilibrated and no accumulation nor axial gradient is present (assumption 6), the concentration of the oxide ions and the vacancies is fixed, and no material balance is accounted for. Instead, the charge balance within the GDC phase is modeled considering the conservation equation in terms of bulk overpotential η, making use of an effective ionic conductivity parameter and evidencing the double layer capacitive current (Eq. 12). Equation 12 is derived by assuming a gradient-less GDC phase, wherein the vacancy flow rate is exclusively due to the electrical migration term. Indeed, setting constant vacancies concentration, the ionic conductivity results constant (Eq. 13). In this way, while the capacitive current is associated to the bulk overpotential, the gradient of ionic current retains a second order dependence on the bulk potential ϕ_E^b of the GDC phase, in accordance with the Ohm's law. As in the case of LSCF, the relation for the vacancy flux in GDC is obtained by substituting the electrochemical potential (Eq. 14) into the definition of the flux density.

$$C_{DL}^{int} \cdot a_v^{int} \cdot \frac{d\eta}{dt} = \sigma_{ion,E}^{eff} \cdot \frac{d^2\phi_E^b}{dz^2} - n_{V_{\ddot{O}}} \cdot F \cdot \left(a_v^{int} \cdot r_4 + \lambda_{TPB} \cdot r_5\right) \qquad (12)$$

$$J_{V_{\ddot{o},E}} = -\frac{z_{V_{\ddot{o}}} F \cdot D_{V_{\ddot{o},E}}^{eff}}{RT} \cdot C_{V_{\ddot{O}},E}^{eq} \cdot \frac{d\phi_E^b}{dz} = -\frac{\sigma_{ion,E}^{eff}}{z_{V_{\ddot{o}}} F} \cdot \frac{d\phi_E^b}{dz} \qquad (13)$$

$$\bar{\mu}_{V_{\ddot{o},E}} = \mu_{V_{\ddot{o},E}}^0 + RT \cdot ln\left(C_{V_{\ddot{O}},E}^{eq}\right) + z_{V_{\ddot{o}}} \cdot F \cdot \phi_E^b \qquad (14)$$

The electronic current density is defined only in the LSCF phase (assumption 8), according to the Ohm's law with adoption of an effective electronic conductivity coefficient (Eq. 15). Due to the mixed conductive properties, the electronic current is

also driven by the bulk potential of LSCF, which is the same potential that appears in the migration term of the vacancies flux.

$$\hat{I}_{e-} = -\sigma_{el,M}^{eff} \cdot \frac{d\phi_M^b}{dz} \qquad (15)$$

In turn, the electronic current density is determined by imposing the condition of local charge conservation within the electrode volume. Namely, in every position along the cathode, the total current density applied at the current collector distributes into the following three channels: the electronic current in LSCF, the ionic current flowing in the LSCF lattice, and the ionic current in the GDC lattice (Eq. 16). The ionic current densities are calculated from the vacancies fluxes following the Faraday's law (Eq. 17).

$$\hat{I}_{e-}^M + \hat{I}_{ion}^M + \hat{I}_{ion}^E = \hat{I}_{tot} \qquad (16)$$

$$\hat{I}_{ion}^M + \hat{I}_{ion}^E = z_{V_{\ddot{o}}} \cdot F \cdot \left(J_{V_{\ddot{o},E}} + J_{V_{\ddot{o},M}}\right) \qquad (17)$$

The electrode potential V_{eld} is defined as the difference between the electrostatic potential of electrons in the current collector and the potential of the electrolyte at the electrode/electrolyte interface. In light of assumption 9, considering the equilibrium between the electrons in the current collector and the electrons in the LSCF, V_{eld} is the difference between the potential of the LSCF and of the GDC measured at each side of the composite cathode (Eq. 18).

$$V_{eld} = \phi_M^b\big|_0 - \phi_E^b\big|_{End} \qquad (18)$$

This definition of the electrode potential is analogous to that proposed in Refs. [41] and [34]. It can be demonstrated (Appendix A) that it leads to an explicit form (Eq. A4) which highlights the contributions of the bulk overpotential, of a concentration overpotential due to ions and vacancies in the MIEC, and of a term

associated to the transport of electronic current. Due to the high electronic conductivity of LSCF and to the modest deviation of oxide ions and vacancies from the equilibrium, the traditional assumption that the electrode potential equals the applied bulk overpotential is attained. This also suggests that the electrode potential is mostly driven by the bulk overpotential between the two phases.

$$V_{eld} = \eta|_{End} + \frac{RT}{2F} \cdot ln\left(\frac{C_{O_{o,M}^{x}}}{C_{V_{\ddot{o},M}}} \cdot \frac{C_{V_{\ddot{o},M}}^{eq}}{C_{O_{o,M}^{x}}^{eq}}\right)\Bigg|_{End} + \left(\phi_M^b\big|_0 - \phi_M^b\big|_{End}\right) \qquad \text{(A4)}$$

The overpotentials and the kinetic rates (Section 3.4) must be specified to complete the model equations. Three overpotentials are required, the bulk overpotential η, the surface overpotential Δχ and the TPB overpotential η_{TPB}. The bulk overpotential is defined as the difference between the bulk potentials of LSCF and GDC (Eq. 19). It is referenced to the equilibrium potential $\Delta\phi^{eq}$ (Eq. 20), defined as the potential at which the net rate of reaction step S4 is zero [49], and which is a function of the local concentration of vacancies and oxide ions, as well as of the equilibrium constant of the reaction k_4^{eq} (Section 3.4).

$$\eta = \phi_M^b - \phi_E^b - \Delta\phi^{eq} \qquad (19)$$

$$\Delta\phi^{eq} = +\frac{RT}{2F} \cdot ln\left(k_4^{eq} \cdot \frac{C_{V_{\ddot{o},E}} \cdot C_{O_{o,M}^{x}}}{C_{V_{\ddot{o},M}} \cdot C_{O_{o,E}^{x}}}\right) \qquad (20)$$

Following the definition provided by Fleig [36] and Liu [38, 40], the surface overpotential Δχ is defined as the difference between the potential ϕ_M^b in the bulk of LSCF and the potential ϕ_M^s at the surface of LSCF. According to the Poisson's law, it is expressed as a function of the surface site density, of the surface capacitance and of the coverage fraction of the adsorbed charged species, i.e. the fraction of the charged oxygen atom (Eq. 21). The overpotential is then derived as the difference between the local surface potential and the equilibrium potential (Eq. 22).

$$\chi = \phi_M^b - \phi_M^s = \frac{\Gamma \cdot F}{C_{DL}^{surf}} \cdot \theta_{O_M^{-}ads} \qquad (21)$$

$$\Delta\chi = \frac{\Gamma \cdot F}{C_{DL}^{surf}} \cdot \left(\theta_{O_M^{-}ads} - \theta_{O_M^{-}ads}^{eq}\right) \qquad (22)$$

Finally, it can be demonstrated [27, 36] that the TPB overpotential is a linear combination of the surface overpotential and of the bulk overpotential (Eq. 23). As pointed out by Zhang et al. [38], the relation stems from the fact that the electrode potential associated to the 2PB pathway must be equal to that associated to the TPB pathway, irrespective of which of the two prevails, for self-consistency. An additional consequence of this relationship is that the equilibrium potential of the TPB step $\Delta\phi_{TPB}^{eq}$ can be derived as a linear combination of the equilibrium potentials $\Delta\phi^{eq}$ and χ^{eq} (Eq. 24).

$$\eta_{TPB} = 2\eta - \Delta\chi \qquad (23)$$

$$\Delta\phi_{TPB}^{eq} = 2\Delta\phi^{eq} - \chi^{eq} \qquad (24)$$

3.3 Boundary conditions

With respect to the concentration of molecular oxygen, a condition of continuity is established at the current collector (z = 0), which describes the recirculation zone adjacent to the electrode as a CSTR (Eq. 25). Considering that the symmetric cell is tested in a stagnation point flow setup, perfect mixing of the incoming gas is assumed in the volume between the inlet supply port and the electrode surface.

$$V_{CSTR} \cdot \frac{dC_{O_2}}{dt} = F^{in} \cdot y_{O_2}\big|_0 - F^{out} \cdot y_{O_2} - J_{O_2}\big|_0 \cdot S_{eld} \qquad (25)$$

The potential of LSCF is fixed at zero at the CC/electrode interface (Eq. 26) and set as the reference. Two conditions are expressed for the potential of the GDC electrolyte. At the current collector, the GDC potential must guarantee that the bulk overpotential is null: as a consequence, it can be calculated directly from the equilibrium potential $\Delta\phi^{eq}$ (Eq. 27). At the electrode/electrolyte interface, the entire current applied to the electrode flows into the electrolyte in form of ions that pass through the GDC phase as well as through the LSCF phase (Eq. 28).

$$\phi_M^b\big|_0 = 0 \qquad (26)$$

$$\phi_E^b\big|_0 = -\frac{RT}{2F}\cdot ln\left(k_4^{eq}\cdot\frac{C_{V_{\ddot{o},E}}\cdot C_{O_{o,M}^x}}{C_{V_{\ddot{o},M}}\cdot C_{O_{o,E}^x}}\Big|_0\right) \qquad (27)$$

$$-\sigma_{ion,E}^{eff}\cdot\frac{d\phi_E^b}{dz}\Big|_{End} + z_{V_{\ddot{o}}}\cdot F\cdot J_{V_{\ddot{o},M}}\big|_{End} = \hat{I}_{tot} \qquad (28)$$

The boundary condition on the molar flux density of the LSCF vacancies (Eq. 29) states that the ionic current is null at the CC. The condition associated to the concentration of the LSCF vacancies is established according to the assumption of no flux also at the CC (Eq. 30).

$$J_{V_{\ddot{o},M}}\big|_0 = 0 \qquad (29)$$

$$\frac{dC_{V_{\ddot{o},M}}}{dz}\Big|_0 = 0 \qquad (30)$$

3.4 Kinetic rate equations

With reference to the kinetic mechanism outlined in Section 3.1, detailed rate equations are written under the assumption that each step is considered elementary.

The rate of O_2 dissociative adsorption (step S1) is modeled according to a Langmuir-type relationship:

$$r_1 = \vec{k}_1 \cdot \Gamma^2 \cdot \theta_F^2 \cdot P_{O_2} - \overleftarrow{k}_1 \cdot \Gamma^2 \cdot \theta_{O_M^{ads}}^2 \qquad (31)$$

Butler-Volmer forms are adopted for the rate equations of the charge transfer reactions. The symmetry factor α is assumed equal to 0.5 for each step. The rates of first electronation S2 (Eq. 32) and second electronation S3 (Eq. 33) depend on the surface overpotential $\Delta\chi$ and are referenced to equilibrium surface potential χ^{eq}. For both these steps, the number of charges transferred n_{e^-} is equal to 1.

$$r_2 = \vec{k}_2 \cdot \Gamma \cdot \theta_{O_M^{ads}}^{eq} \cdot exp\left(-\frac{\alpha \cdot n_{e^-} \cdot F \cdot \chi^{eq}}{RT}\right) \cdot$$

$$\cdot \left[\frac{\theta_{O_M^{ads}}}{\theta_{O_M^{ads}}^{eq}} \cdot \exp\left(-\frac{\alpha \cdot n_{e^-} \cdot \mathrm{F} \cdot \Delta\chi}{RT}\right) - \frac{\theta_{O_M^{-ads}}}{\theta_{O_M^{-ads}}^{eq}} \cdot \exp\left(+\frac{(1-\alpha) \cdot n_{e^-} \cdot \mathrm{F} \cdot \Delta\chi}{RT}\right)\right] \qquad (32)$$

$$r_3 = \vec{k}_3 \cdot \Gamma \cdot \theta_{O_M^{-ads}}^{eq} \cdot C_{V_{\ddot{O}},M}^{eq} \cdot exp\left(+\frac{\alpha \cdot n_{e^-} \cdot F \cdot \chi^{eq}}{RT}\right) \cdot$$

$$\cdot \left[\frac{\theta_{O_M^{-ads}}}{\theta_{O_M^{-ads}}^{eq}} \cdot \frac{C_{V_{\ddot{O}},M}}{C_{V_{\ddot{O}},M}^{eq}} \cdot exp\left(+\frac{\alpha \cdot n_{e^-} \cdot \mathrm{F} \cdot \Delta\chi}{RT}\right) - \frac{\theta_F}{\theta_F^{eq}} \cdot \frac{C_{O_{O,M}^x}}{C_{O_{O,M}^x}^{eq}} \cdot exp\left(-\frac{(1-\alpha) \cdot n_{e^-} \cdot \mathrm{F} \cdot \Delta\chi}{RT}\right)\right] \qquad (33)$$

Following the work of Mebane and Liu [40], while the first electronation is promoted by an increase of surface overpotential, the second electronation is adversely affected. It is also noted that, although the definition of the equilibrium potential does not stem from a Nernst-type relationship rather from the Poisson's law, the thermodynamic consistency of both equations is retained as the rates become null when the electrode reaches the equilibrium with respect to the LSCF surface coverage and to the concentration of oxide ions and vacancies.

The rate of step S4, i.e. the transport of oxide ions across the LSCF/GDC interface, is referenced to the difference of bulk potentials at the equilibrium $\Delta\phi^{eq}$ and is a function of the bulk overpotential η (Eq. 34). The relationship is written considering that both the vacancies and the oxide ions of the GDC phase are equilibrated under all the operating conditions explored (assumption 6). The number of charges transferred $n_{V_{\ddot{O}}}$ is equal to 2.

$$r_4 = \vec{k}_4 \cdot C_{O^x_{o,M}}^{eq} \cdot C_{V_{\ddot{O},E}}^{eq} \cdot exp\left(-\frac{\alpha \cdot n_{V_{\ddot{O}}} \cdot F \cdot \Delta\phi^{eq}}{RT}\right) \cdot$$

$$\cdot \left[\frac{C_{O^x_{o,M}}}{C^{eq}_{O^x_{o,M}}} \cdot exp\left(-\frac{\alpha \cdot n_{V_{\ddot{O}}} \cdot F \cdot \eta}{RT}\right) - \frac{C_{V_{\ddot{O},M}}}{C^{eq}_{V_{\ddot{O},M}}} \cdot exp\left(+\frac{(1-\alpha) \cdot n_{V_{\ddot{O}}} \cdot F \cdot \eta}{RT}\right)\right] \quad (34)$$

Finally, the rate associated to the three phase boundary reaction (S5) is a function of the TPB overpotential η_{TPB} and is referenced to the corresponding equilibrium condition $\Delta\phi^{eq}_{TPB}$ (Eq. 24).

$$r_5 = \vec{k}_5 \cdot \Gamma \cdot \theta^{eq}_{O^-_M ads} \cdot C_{V_{\ddot{O},E}}^{eq} \cdot exp\left(-\frac{\alpha \cdot n_{e^-} \cdot F \cdot \Delta\phi^{eq}_{TPB}}{RT}\right) \cdot$$

$$\cdot \left[\frac{\theta_{O^-_M ads}}{\theta^{eq}_{O^-_M ads}} \cdot exp\left(-\frac{\alpha \cdot n_{e^-} \cdot F \cdot \eta_{TPB}}{RT}\right) - \frac{\theta_F}{\theta_F^{eq}} \cdot exp\left(+\frac{(1-\alpha) \cdot n_{e^-} \cdot F \cdot \eta_{TPB}}{RT}\right)\right] \quad (35)$$

3.5 Thermodynamic properties

The thermodynamic consistency of the kinetic scheme requires the equilibrium constant of each step to be known [50, 51]. The formation enthalpy ΔH_i^F and the absolute entropy S_i^0 of each species are used to calculate the Gibbs free energy of each reaction step. Their values and source are reported in Table 4. In order to limit the number of parameters to be fitted, as many literature values as available are

adopted. Additionally, electrons, free sites, LSCF vacancies and GDC vacancies are set as reference species, so that the corresponding formation enthalpies and absolute entropies are null in the whole temperature range.

The formation enthalpy and the absolute entropy of molecular O_2 are calculated as a function of the temperature, based on a standard database for thermodynamic properties [52]. The formation parameters of the oxide ion within the LSCF lattice are calculated from the data reported by Bishop et al. [53] in their work dedicated to surface and bulk equilibria in LSCF samples. Specifically, the reaction enthalpy ΔH_{ox} and entropy ΔS_{ox} of the LSCF oxidation reaction (Eq. 36) in the itinerant metallic equilibrium model is assumed, which amount respectively to -104 kJ/mol and -65.7 J/mol/K.

$$\frac{1}{2}O_2 + V_{\ddot{O},M} + 2e^- \leftrightarrow O_{O,M}^x \qquad (36)$$

Notably, the enthalpy of the oxidation reaction is taken as constant over the temperature range explored: considering the assumption of null thermodynamic parameters for vacancies and electrons, the formation parameters of the oxide ion vary with temperature. Nonetheless, this variation never exceeds 10% and negligibly affects the calculations, amounting to +5.2 kJ/mol over -93.1 kJ/mol going from 560°C to 700°C, and +5.6 J/mol/K over +55 J/mol/K in the case of the absolute enthalpy.

In the case of the formation of oxide ions in the GDC lattice, the parameters provided by Yurkiv et al. [10] are assumed. In the literature, wide agreement [54, 55] is found upon that the enthalpy of oxidation ΔH_{ox} of Ce^{3+} oxide in GDC at 10% doping (Eq. 37) amounts to -440 kJ/mol per mol of lattice oxygen. More scattered estimates are found in the case of the reaction entropy ΔS_{ox}, ranging from -270 J/mol/K reported by Wang et al. [54] to -127 J/mol/K reported by Bishop et al. [56].

The parameters reported in Table 4 (-200 kJ/mol and +70 J/mol/K) imply that cerium ions are not reference species, rather possess individual and distinct formation enthalpies and absolute entropies, which do not sum to zero. Hence, in the absence of reliable estimates of these latter parameters, the thermodynamic consistency cannot be readily verified based on measured values of ΔH_{ox} and ΔS_{ox}.

$$\frac{1}{2}O_2 + V_{\ddot{O},E} + 2Ce'_{Ce} \leftrightarrow O^x_{O,E} + 2Ce^x_{Ce} \qquad (37)$$

The formation enthalpy of the oxygen atom adsorbed on the LSCF surface (-83.2 kJ/mol) is calculated starting from the DFT estimation of -188.1 kJ/mol O_2 (-1.95 eV) provided by Choi et al. [57] for LSC surfaces. It shall be noted that this choice is conservative, since a much lower adsorption enthalpy (-0.9 eV) is reported by the same authors in the case of LSF surfaces. Nonetheless, the formation enthalpy obtained is in close agreement with that used by Yurkiv et al. [10] for LSCF (-83.5 kJ/mol). Instead, no reference values are found for the absolute entropy of O_M^{ads}. A null value is then attributed to this parameter in order to avoid fitting.

The thermodynamic properties of the adsorbed single-charged oxide ion are not easily found in the literature, due to the absence of direct measurements. A first estimate is provided by Yurkiv et al. [10] for the formation enthalpy of O_M^{-ads}, calculated by data fitting. In agreement with the same authors, the absolute entropy $S^0_{O_M^{-ads}}$ is assumed equal to zero, so that the number of unknown values maintains reasonably limited.

3.6 Equilibrium composition

The Butler Volmer form of the reaction rates requires the knowledge of the equilibrium composition under all the temperature and O_2 pressure levels explored.

Considering that, under OCV, the current density drawn is null and that both the axial gradient and the oxygen conversion are negligible, for each species the equilibrium values are maintained constant along the axis of the cathode. In the case of surface species coverages, the equilibrium constraints Eq. (38) and (39) are solved together with the equation of conservation of the active sites (Eq. 6). The equations retain a dependency on the equilibrium surface potential χ^{eq}, which in turn is calculated via Eq. 21 with $\theta^{eq}_{O_M^{-}ads}$. As a consequence, on the one hand, the relationships are implicit. On the other hand, consistently with the presence of a potential barrier against electronation, the larger χ^{eq} is, the smaller the coverage fraction of charged oxygen adatoms becomes at the equilibrium. The coverage fraction of charged oxygen adatoms (Table 5) always maintains around 1% under all the investigated conditions, in line with the values reported in the literature by other authors [38, 39]. Correspondingly, the equilibrium surface potential sets between 50 and 150 mV.

$$\theta^{eq}_{O_M^{ads}} = \frac{\sqrt{k_1^{eq}\cdot P_{O_2}}}{1+\left[1+k_2^{eq}\cdot exp\left(-\frac{n_{e^-}\cdot F\cdot \chi^{eq}}{RT}\right)\right]\cdot\sqrt{k_1^{eq}\cdot P_{O_2}}} \quad (38)$$

$$\theta^{eq}_{O_M^{-}ads} = \frac{k_2^{eq}\cdot\sqrt{k_1^{eq}\cdot P_{O_2}}\cdot exp\left(-\frac{n_{e^-}\cdot F\cdot \chi^{eq}}{RT}\right)}{1+\left[1+k_2^{eq}\cdot exp\left(-\frac{n_{e^-}\cdot F\cdot \chi^{eq}}{RT}\right)\right]\cdot\sqrt{k_1^{eq}\cdot P_{O_2}}} \quad (39)$$

An equilibrium relationship (Eq. 40) is also used to calculate the concentration of vacancies in the LSCF phase. The equation takes into account the conservation of lattice oxygen ions and assumes that the activity of electrons is unitary.

$$C^{eq}_{V_{\ddot{O}},M} = \frac{C_{mc,M}\cdot\theta_F^{eq}}{\theta_F^{eq}+k_3^{eq}\cdot\theta^{eq}_{O_M^{-}ads}\cdot exp\left(+\frac{n_{e^-}\cdot F\cdot \chi^{eq}}{RT}\right)} = \frac{C_{mc,M}}{1+k_3^{eq}\cdot k_2^{eq}\cdot\sqrt{k_1^{eq}\cdot P_{O_2}}} \quad (40)$$

The vacancies concentration retains a dependency on P O_2 equal to -0.5, which stems from the original step of O_2 dissociative adsorption and is consistent with a mass

action type law. Notably, the relationship predicts a growth of vacancies with decreasing O_2 partial pressure, as well as with an increase of temperature, which is in line with common measurements under equilibrated conditions [53, 58]. A dependency equal to -0.5 is also reported by Bishop et al. [53] both numerically and experimentally for P $O_2 > 10^{-2}$ atm, well within the limits of the present analysis.

The concentrations of vacancies and oxide ions in GDC are fixed to the stoichiometric amounts, and are maintained constant with temperature and pressure. At 10% gadolinia doping and considering a fluorite structure, the stoichiometric concentration of vacancies $C_{V_{\ddot{o},E}}^{eq}$ (2.1×10^3 mol/m^3) amounts to 2.5% of the concentration of total stoichiometric oxygen of the lattice $C_{mc,E}$, which is 8.33×10^4 mol/m^3. The concentration of lattice oxygen is calculated as the difference, according to the charge balance. The choice of adopting stoichiometric concentrations is coherent with the fact that ceria works under high oxygen partial pressure in the experiments (log P $O_2 > 10^{-2}$). In turn, this means that no extra vacancies are formed with respect to the intrinsic stoichiometric amount due to the gadolinia doping, and also that GDC acts exclusively as a vacancy vector thanks to its high ionic conductivity. An additional consequence of this choice is that the energetic parameters of Table 4 are used only to guarantee the thermodynamic consistency of step S4 of the kinetic scheme. Indeed, calculations based on equilibrium constraints lead to an almost null concentration of over-stoichiometric vacancies in GDC, due to the very exothermic formation enthalpy of oxide ions.

3.7 Morphologic, structural and transport parameters

Following the guidelines reported by Chen et al. [47] for binary mixtures, the percolation theory is applied to calculate the electrode's main structural parameters,

based on the measured values of particle size, porosity and volume fractions (Table 1). Although a distribution of sizes is observed, a single value (0.8 μm) identical for both LSCF and GDC particles is used in the calculations. A specific interfacial area a_v^{int} of 9.41×10^4 m^2/m^3 and a TPB extension λ_{TPB} of 1.82×10^{12} m/m^3 are estimated. The specific adsorption area a_v^{ads} (2.38×10^6 m^2/m^3) is calculated as that of a packed bed of spheres multiplied by the volume fraction of LSCF in the mixture, which amounts to 53%. Comparable values of λ_{TPB} (3.4×10^{12} m/m^3) and a_v^{ads} (9.9×10^5 m^2/m^3) are measured by He et al. [59, 60] via FIB-SEM tomographic reconstruction of LSCF-GDC 50/50 electrodes with similar particle size (0.6 μm) and porosity, which suggest that the calculated parameters are reasonable. A wide scatter of experimental estimates is however found in the literature, due to differences in preparation and deposition techniques, and in thermal treatments applied to achieve the final target structure.

A different method is required to calculate the double layer capacitance C_{DL}^{int} and the surface capacitance C_{DL}^{surf} (Table 2). The double layer capacitance, which is directly related to the local charge distribution in the contact region between GDC and LSCF and ultimately to the morphology of the interface, is reported to vary according to an activated Arrhenius type relationship [61]. The associated values (pre-exponential factor and activation energy) are estimated by fitting to the experimental Bode curves, which are especially sensitive to the capacitance. An additional parameter is introduced, which is the exponent γ_{CPE} of the constant phase element [62]. In order to take into account the distribution of characteristic times associated to capacitive phenomena, the double layer capacitance is treated as a CPE element (Appendix B), which asks for estimating the exponent γ_{CPE}. This latter term is understood as an indicator of the non-ideality of the microstructure of the LSCF/GDC interface: it is also calculated by fitting, being equal to 1 in case of an ideal capacitor.

The surface capacitance is associated to the local roughness of the LSCF surface: several authors adopt a constant value, independent of the electrode temperature. A relation is also proposed, which is derived by assuming that the gas/electrode interface can be treated as flat plate capacitor. In the case of LSCF, two main values of C_{DL}^{surf} are reported in the literature, namely 100 F/m^2 [10, 43, 63], which is estimated by fitting to experimental data, and 0.1 F/m^2, which is based on physic relations of dipole moment and double layer capacitance [27, 33, 36, 38, 39]. It is important to note that the value adopted in Table 2 (0.1 F/m^2) leads to a small coverage fraction of charged oxygen adatoms O_M^{-ads} at equilibrium (Table 5), consistently with the assumption required by the application of equation 21. Instead, the adoption of the larger surface capacitance would have resulted in much higher $\theta_{O_M^{-ads}}^{eq}$ (~10% at 560°C), in conflict with the definition of the surface potential χ.

The ionic conductivity of bulk GDC is derived from the ohmic resistance measured in the EIS experiments (Fig. 5b and Table 2). Compared to the reference equation provided by Steele [64] ($1.09 \times 10^5/T \times \exp(-61.7 \times 10^3/R/T)$ S cm^{-1}), the activation energy is moderately higher (69.7 kJ/mol vs. 61.7 kJ/mol) and the conductivity values result almost halved (2.3×10^{-2} vs. 5.5×10^{-2} S cm^{-1} at 700°C). This is consistent with the presence of unavoidable contact resistances and local imperfections in the handmade pellet, as well as with the fact that the relation of Table 2 takes into account the grain boundary resistance, and does not exclusively describe the intrinsic properties of the material. The effective ionic conductivity of the GDC particles in the electrode matrix $\sigma_{ion,E}^{eff}$ is calculated starting from the measured bulk property applying percolation theory correlations for binary mixtures. The effective parameter (Eq. 42) used in the model is a function of the microstructural features of the electrode (Table 1), specifically the volume fraction of the GDC particles f_E and the percolation

probability number P_E. This probability is estimated according to equation 43, which is based on the average contact number between GDC particles $Z_{E,E}$ [65]. As a matter of fact, the effective conductivity reduces to 12% of the bulk conductivity.

$$\sigma_{ion,E}^{eff} = \sigma_{GDC}^{ion} \cdot [(1-\varepsilon) \cdot f_E \cdot P_E]^{1.5} \qquad (41)$$

$$P_E = 1 - \left(\frac{3.764 - Z_{E,E}}{2.472}\right)^{3.7} \qquad (42)$$

Aside of the ionic conductivity of GDC, literature correlations are adopted to calculate the transport properties as a function of temperature. All these properties are considered independent of the oxygen partial pressure. The equation for the electronic conductivity of LSCF is derived based on the values measured by Stevenson et al. [66]: the simple linear correlation evidences the metallic nature of the conductivity in the temperature range of interest, which decreases when passing from 560°C to 700°C. Several experimental works have been dedicated to the measurement of the vacancy diffusion coefficient in LSCF, and more than an order of magnitude range is found among the various measurements. The scatter of this coefficient is due to differences in pretreatment and preparation procedures, real stoichiometry of the material, thermal and chemical history of the sample and, above all, progress of the degradation process [4]. The thermodynamic factor A is also widely discussed both in terms of functional dependence and correlation [42]. As a matter of fact, this factor can be reasonably taken as constant, given that it shows a very weak dependence on P O_2 between 1 and 10^{-1} bar and a relatively small range of oxygen partial pressure is considered. Under this assumption, in equation 43, which defines the relationship between the vacancies chemical diffusion coefficient $D_{V_{\ddot{o},M}}^{\delta}$ and the vacancies self-diffusion coefficient $D_{V_{\ddot{o},M}}$, the thermodynamic factor A retains only the dependency

on temperature, and the correlation provided by Endler-Schuck et al. [12] is applied, which is based on experiments in air.

$$D^{\delta}_{V_{\ddot{o},M}} = A \cdot D_{V_{\ddot{o},M}} \qquad (43)$$

The chemical diffusion coefficient is estimated with a correlation extracted from the work of Bowmesteer et al. [58] and confirmed by the group of Ivers-Tiffeè in more recent works [12, 21]. An activation energy of 121 kJ/mol and a pre-exponential factor of 5.8×10^{-4} m^2/s are derived from the original data, which result in a chemical diffusion coefficient of 1.82×10^{-10} m^2/s at 700°C. Also in this case, the correlation for $D^{\delta}_{V_{\ddot{o},M}}$ in Table 2 refers to the intrinsic property. The effective diffusivity is a function of the electrode's morphology ($Z_{M,M}$ and f_M, Table 1), and is calculated with equations 41 and 42. Compared to the intrinsic diffusivity coefficient, a 70% reduction is estimated (i.e. 5.46×10^{-11} m^2/s at 700°C). The value of the self-diffusion coefficient $D_{V_{\ddot{o},M}}$ is calculated with Eq. (43), after estimation of the thermodynamic factor A.

3.8. Numerical method and regression

The set of model equations leads to a differential and algebraic system (DAE), composed of 10 partial differential equations and 5 algebraic equations. The current density at the current collector $\hat{I}_{tot}$ is taken as the input and the electrode potential V_{eld} is calculated. The axial electrode coordinate is divided into a suitable number of grid points, and the spatial derivatives are approximated by the Euler differentiation method in each grid point. Independency of the solution from the grid spacing is achieved with 100 points. The integration of this DAE system in the time domain, although feasible, leads to computing times for a single impedance arc which are

incompatible with the application of a regression routine. A frequency domain transformation method is therefore applied to solve the dynamic problem and cut the computational time, so that the repeated solutions required by the regression can be completed in a reasonable time. Full details on the procedure are reported in Ref. [63]. Here it is convenient to recall that this procedure requires first to find the steady state solution of the DAE system. This is reduced to a linear system by application of the method of lines. Then, instead of solving the DAE system as a function of time forced by an harmonic current input, the frequency domain transformation is applied and a linear complex system is obtained by linearization of the equations around the steady state solution. The harmonic problem is solved in terms of perturbated variables, allowing for the direct computation of the impedance as a function of the frequency [62, 63]. The linearized complex form of each model equation is reported in Appendix B. The code is developed in Matlab. The parameter calibration is performed with a complex non-linear fitting procedure by means of the Levenberg-Marquardt algorithm (lsqnonlin function). The object function minimizes the weighted sum of squared residues calculated on both the real part and the imaginary part of the spectra (Eq. 44). For each experimental data set, the electrode's polarization resistance R_{Pol} (taken as the difference between the intercepts at low frequency and high frequency) is used as the weight $W_{k,r}$ of the real part (Eq. 45). The maximum imaginary impedance value is adopted as the weight $W_{k,i}$ in the case of the imaginary part (Eq. 46). The confidence interval of the fitted parameters is set at 95%. The goodness of the fit is evaluated by visual inspection of the match between the simulated curves and the measured spectra, by evaluation of the correlation matrix, and by performing a χ^2 test based on the experimental variance.

$$SSR = \sum_{k=1}^{N_{data}} \frac{\left[Z_{Real}^{calc}(\omega_k) - Z_{Real}^{exp}(\omega_k)\right]^2}{W_{k,r}^2} + \sum_{k=1}^{N_{data}} \frac{\left[Z_{Im}^{calc}(\omega_k) - Z_{Im}^{exp}(\omega_k)\right]^2}{W_{k,i}^2} \qquad (44)$$

$$W_{k,r} = R_{Pol} \quad (45)$$

$$W_{k,i} = \left|max\left(Z_{Im}^{exp}\right)\right| \quad (46)$$

One target of the work is the use of as many literature data as possible in order to limit the number of unknown parameters to be determined by fitting. On the one hand, this choice leads to more robust estimates of the parameters; on the other hand, it confers the model a higher reliability, and avoids achieving reasonable predictions exclusively due to a high number of degrees of freedom. As a matter of fact, 13 parameters are fitted to the data, namely: the 5 pre-exponential coefficients and the 5 activation energies of the direct steps of the ORR mechanism (Table 3), the exponent of the constant phase element, the pre-exponential factor and the activation energy of the double layer capacitance. The first ten parameters are fitted to the impedance spectra in the Nyquist plots, while the latter three are fitted to the Bode plots, given that the double layer capacitance primarily influences the position of the imaginary curve in the frequency domain.

4. Results

The numerical procedure entails two complete data sets. The first one is derived from inhouse impedance experiments at varying temperature and feed gas composition, and it is used to extract the kinetic parameters and the capacitance parameters by fitting to Nyquist and Bode plots. The second one is taken from the work of Nielsen et al. [6] and it is applied to validate model, by simulating impedance spectra measured in air between 800°C and 600°C.

4.1 Experiments on the inhouse cell

Figure 3 displays the impedance spectra collected at varying temperature and oxygen partial pressure, compared with the model simulations. Figure 4 shows the associated Bode plots. As expected, the preliminary analysis of the spectra reveals that the polarization resistance increases when decreasing temperature and O_2 partial pressure, as a consequence of slower kinetic rates. The shape of the arcs is complex and suggests the presence of multiple concurrent phenomena. At 700°C and 650°C, depressed arcs are observed, while at 650°C and 600°C the shape of the arcs closely resembles that of a Gerischer spectrum, which is typical of semiconducting materials. Upon decreasing the partial pressure of O_2, an additional small arc appears at 700°C at low frequencies (< 10 Hz), which grows passing from 10% to 5% O_2 fraction. This arc can be unambiguously associated to mass diffusion, by comparing the tests performed in N_2 and that in He: as apparent in Figure 5a, the arc disappears when He is used as the O_2 diluent, while full overlap is achieved at 21% O_2 amount. In line with the association to mass transport, which is weakly dependent on temperature (and therefore maintains almost constant), the impact of this arc is smaller at 650°C and negligible below. Under all the examined conditions, the Bode plots show a single main peak, which shifts to lower frequencies when either the O_2 partial pressure or the temperature decreases. Also in this case, the observation is consistent with the slower kinetic rates, which lead to higher characteristic times. At 700°C and air supply, the main peak is centered at 150 Hz, and moves to 60 Hz at 5% O_2, where a second shoulder, associated to the diffusive arc is also noted. The peak shifts to 120 Hz at 650°C, then to 100 Hz at 600°C and reaches 80 Hz at 560°C.

The model simulations, reported as solid lines in the figures, fairly describe the impedance spectra. At 700°C and 650°C, the Nyquist plots are closely matched, with minor deviations in the case of the diffusive arc, possibly due to the simplified treatment of the fluid dynamic pattern outside the electrode and of the current

collector. Upon decreasing the temperature, the main features of the arcs are respected: the polarization resistance in air is always closely captured, so as the shape of the arcs, which turns to a Gerischer like impedance below 600°C. In these latter case, the non-ideality of the microstructure leads to high-frequency asymptotes that are slightly smaller than the theoretical $\pi/4$. An acceptable 4% deviation is found only at 600°C when the oxygen fraction is reduced to 5% (1.06 Ω cm^2 vs. 1.02 Ω cm^2).

In the case of the Bode plots, the shift of the main peak is correctly predicted, although offsets are observed when decreasing the temperature, with a maximum error in the experiment at 5% O_2 (28 Hz vs. 66.6 Hz). These differences are due to the fact that the surface capacitance is taken as constant to limit the number of unknown parameters, while in principle it varies with the temperature. A closer match with the data could be then achieved by tuning also C_{DL}^{surf} at each temperature level.

The model simulations also allow to associate the diffusive arc observed at 700°C and 5% O_2 in N_2 to the effect of external mass transport limitations. On the one hand, if the characteristic frequency of intraporous diffusion is calculated ($f = D_{O_2}^{eff}/L^2$, with $D_{O_2}^{eff}$ = 0.11 cm^2/s and L = 70 µm), a frequency of 2.2 kHz results, which falls largely outside the 0.1 – 1 Hz range of the measured arc (Fig. 5a). On the other hand, it is possible to show by simulation that this arc is due to the fluid dynamic profile established next to the electrode. The spectrum at 5% O_2 dilution is simulated considering He to balance, and substituting the CSTR boundary condition (Eq. 26) with a simplified boundary condition ($y_{O_2}\big|_0$ = 0.05) that excludes any hold-up effect. The simulation obtained under these condition does not predict the second arc at low frequency and matches the spectrum measured in He (Fig. 5c). If the CSTR condition is retained, the simulation in He completely overlaps the simulation in N_2. For this reason, the model results indicate that diffusion limitations are external to the

electrode, likely caused by the stagnation point flow geometry and by the thick current collecting mesh.

4.2 Significance of the fitted parameters

Table 6 reports the correlation matrix of the fitted parameters. The coefficients of this matrix are indicators of the reciprocal influence between two parameters: the higher the value, the more important is the correlation and the less efficient is the fitting procedure. A generally accepted threshold to evaluate the correlation is ±0.8: smaller or larger values indicate that the two parameters have the same effect on the simulation and no distinction can be made. The results show that almost all the parameters are well below this threshold, confirming the goodness of the procedure. One exception is noted, although still close to the limit: the pre-exponential factor of the interfacial capacitance $C_{DL}^{int,0}$ is correlated to the γ_{CPE} factor. This result is in line with the fact that $C_{DL}^{int,0}$ and γ_{CPE} both influence the placement of the peak in the Bode plot in terms of frequency, and partially act in the same way.

The kinetic parameters obtained after fitting are reported in Table 3. The dissociative adsorption step shows the same activation energy (21 kJ/mol vs 20 kJ/mol), which is also identical to that indicated in Ref. [27] for oxygen dissociation on the LSM surface (22.1 kJ/mol, mechanism 2). Similar kinetic parameters are obtained with respect to the first electronation step, which has an activation energy of 196 kJ/mol, in line with 181.4 kJ/mol proposed by Yurkiv et al. [10], and a pre-exponential factor of 5.9×10^{14} s^{-1}, which also fairly agrees with the value of 2.4×10^{13} s^{-1} found by the same authors. With respect to the kinetics of steps 3, 4 and 5, no direct comparison is possible, since these steps are not included in published schemes dedicated to LSCF/GDC electrodes. It is however worthy to note that the activation

energy of the charge transfer steps, either involving ions or electrons, is in line with the apparent activation energy of 130 kJ/mol derived from the ASR (Fig. 5b): this value is a global indicator which groups and averages the effects of ion transfer (much less activated, ~70 kJ/mol) and charge transfer steps, which are then expected to require high activation barriers. Comparatively, the kinetic parameters available in the literature for analogous elementary steps on LSM-YSZ composites indicate that the energy barrier of the first and second electronation or oxide ion inclusion span between 150 and 190 kJ/mol. Close values are found in the case of the TPB step (S5), namely 146.1 kJ/mol vs. 154 – 144 kJ/mol calculated by Banerjee and Deutschmann [27] for different mechanisms. Overall, a global look at the kinetic parameters suggests that they are consistent with other detailed schemes dedicated to the ORR mechanism.

4.3 Model validation

The reliability of the model and of the kinetic parameters is tested by simulation of literature data. The work by Nielsen et al. [6] provides an extensive experimental analysis of LSCF-GDC composite cathodes at varying temperature between 550°C and 850°C in air and OCV conditions. The samples are analogous to those analyzed in the present work, and consist of 50 wt% LSCF 50 wt% GDC at 10% Gd doping, supported by GDC electrolytes. Three datasets are presented, distinguished by the microstructure, which is defined as coarse, moderately coarse, and fine. The model validation is performed based on the moderately coarse electrode for two reasons. On the one hand, in the original paper [6], this sample was prepared according to the same thermal treatment followed in the present work (exposure to 1000°C for 2 h), while the coarse structure was achieved by exposure to higher

temperature, which likely led to a modification of the material properties together with the microstructure. As a matter of fact, if the area specific resistances are compared, the coarse electrode shows a larger activation energy than the moderately coarse electrode (160 kJ/mol vs. 131 kJ/mol), which suggests that the ORR kinetics changed. On the other hand, the fine microstructure falls in the limit that breaks down one-dimensional continuum model approaches, and would require a detailed description of the local microstructure [16, 21]. With respect to this latter point, the quantitative criterion presented by Fleig [37] highlights that most of the data from the fine-structured electrode belongs to polarization regimes where an approach based on finite volumes is more appropriate.

Table 7 lists the parameters used to simulate the spectra collected on the moderately coarse sample. The SEM picture of the electrode shows a 12 μm thick layer, with an average pore size ≤ 0.5 μm. A porosity of 40% is estimated, which is associated to a tortuosity of 2.5. Since no clear distinction between LSCF and GDC particles can be inferred, the specific surface of LSCF a_v^{ads}, the specific interfacial surface a_v^{int}, and the TPB length λ_{TPB} are taken as tuning parameters. Nonetheless, in order to limit the degrees of freedom, their value is obtained by diving those of Table 2 by a common factor, fitted exclusively to the arc measured at 750°C. This scaling factor amounts to 1.27, meaning that a 22% reduction of the morphologic parameters is required to match the arc at 750°C. As no pieces of information are provided on the molar flow rate, the experiments are simulated by assuming a simplified boundary condition on molecular O_2 ($y_{O_2}\big|_0 = 0.21$), which is fully valid at OCV when no gas diffusion impedance occurs. No tuning is performed on the exponent γ_{CPE} of the constant phase element, which is assumed to be equal to 1. The literature correlation by Steele [64] is applied to calculate the ionic conductivity of GDC.

The comparison between simulations and data is reported in Figure 6. Close match is achieved between 650 and 800°C, while overestimation is observed at 850°C and 600°C. The model correctly describes the series of Gerischer arcs: the initial $\pi/4$ high frequency branch is always respected and the general shape of the spectra is reproduced. The kinetic scheme holds outside its original tuning temperature range up to 800°C, suggesting that the energetic parameters are robust in terms of activation energies and thermodynamics. Coming to the deviations, the offset is 9.7% at 600°C (0.82 Ω cm^2 vs. 0.90 Ω cm^2) and 18% at 850°C (0.0165 Ω cm^2 vs. 0.014 Ω cm^2). Their nature is however different. In the first case, it appears that the model anticipates the transition between a Gerischer-type arc and an arc shaped with the $\pi/4$ high frequency branch followed by a semicircle: specifically, such transition occurs when the characteristic electrochemical length becomes larger than the electrode thickness, and kinetically limits the ORR. Under this condition, a steep increase of the polarization resistance and a high sensitivity are observed upon varying the electrode's thickness (Section 5.1). If the electrode thickness is increased to 14 μm (the original SEM picture of the electrode shows a thicker zone), a closer match is realized in terms of shape and polarization resistance (dashed line in Fig. 6f). In the case of the experiment at 850°C, a better refinement of the morphologic properties for the composite (i.e. the additional independent tuning of the TPB length and of the interfacial specific area) allows matching the experimental data. Overall, however, the simulations satisfactorily describe the dataset, and provide a fair validation of the model.

4.4 Sensitivity analysis

The results of a sensitivity analysis (SA) on the kinetic and morphologic parameters are reported in Figure 7, in the case of air supply for all the temperature levels. A sensitivity index (SI) is calculated based on the change of the polarization resistance R_{Pol} due to a ±10% variation of each parameter. Negligible differences in the SI values are found when moving from air to smaller O_2 partial pressures, which allow to assume the results in air as representative of all the others. Similarly, the kinetic analysis is performed only on the pre-exponential factors, since the results obtained by changing the activation energies are analogous. At 700°C, the kinetics of step S2 (the first electronation of the oxygen adatom) and step S5 (the reaction between one charged oxygen adatom and a GDC vacancy at the TPB) concurrently lead to the highest variation of R_{Pol}, showing similar SI values (±20% for S2 and ±18% for S5). The other steps are much less kinetically relevant, suggesting that the first electronation and the TPB transfer reaction co-limit the ORR process. Coming to the transport parameters, the SA highlights that the ionic conductivity of GDC σ_{GDC}^{ion} shows a most important sensitivity index, whereas both the vacancy diffusion $D_{V_{\ddot{o},M}}$ and the electronic conductivity σ_{LSCF}^{ele} of LSCF are insensitive. These results allow to draw a neat picture of the kinetic mechanism that drives the ORR from molecular O_2 up to the formation of an oxide ion in the GDC lattice, and evidence that the main transport route is the TPB pathway. Namely, LSCF activates molecular oxygen by providing the adsorption sites and by quickly supplying the first electron: the formation of the first charged species, the oxygen adatom, is followed by transfer to the interface with GDC and inclusion in its lattice. In turn, the GDC phase retains a key role in transporting the oxide ion towards the solid electrolyte, acting as a pipe for oxide ions, as suggested by the high SI associated to its conductivity. Moving from a pure LSCF electrode to a composite structure by addition of GDC improves the cathode performance by providing a faster channel to transport ions on longer

distances: instead of being forced to move within the LSCF lattice across the whole electrochemically active length, a more effective transport occurs in the GDC phase. This result is in line with those of Laurencin and coworkers [33], who show that the TPB prevails over the 2PB in LSCF-GDC composites at OCV in a similar temperature range (750 – 650°C).

Interpreting the effects of the morphologic parameters is straightforward. Upon decreasing either the porosity or the particle size, a reduction of R_{Pol} is observed since the TPB length λ_{TPB} and the specific adsorption area a_v^{ads} both increase. In turn, these two parameters act as multiplying factors of the TPB rate and the electronation rate in conservation equations. The reduction of the electrode porosity also increases the effective GDC conductivity, leading to an additional boost of the performance. For similar reasons, being a multiplier of the kinetic rates (Eq. 32 and 35), a growth of the surface sites concentration Γ has a beneficial impact. Notably, the particle size and the porosity show the largest sensitivity index, suggesting that the accurate determination of the adsorption area and of the TPB extension is a pre-requisite of primary importance when estimating the pre-exponential factors of the kinetic rates. Given that these latter scale linearly with λ_{TPB}, a_v^{ads} and a_v^{int}, an error bar can be estimated based on the results of the granulometry test (Fig. 1c): if the central 40% share of the particle size distribution is considered (0.5 – 1.1 µm, neglecting the side shoulder), by calibrating the model at the two limits of the interval, a ±37% variation is estimated for $\vec{k}_2$, $\vec{k}_3$ and $\vec{k}_4$, while the variation rises to ±60% in the case of $\vec{k}_5$ (Table 4). Increasing the electrode thickness is also found to reduce R_{Pol}. This effect (discussed in Section 5.2) is due to the increase of the overall extent of the active area: in this case, it is important to note that the measurements are collected at OCV, and that gas diffusion is absent in the presence of air and very limited when the partial pressure of oxygen is reduced to 5% (~2×10^{-2} Ω cm^2, Fig. 5a). As a consequence,

increasing the electrode thickness does not lead to an increase of concentration polarization.

Moving from 700°C to 560°C, the kinetic picture partially modifies. The importance of the first electronation step progressively decreases in favor of the TPB step, which becomes determining (RDS). Simultaneously, the effects of the second electronation (S3) and of the oxide ion transfer at the LSCF/GDC interface (S4) moderately but steadily grow: these results indicate that the 2PB route partially activates upon decreasing the temperature, although remaining a minor contribution. Form a model viewpoint, this is exclusively a consequence of the different activation energies of the kinetic rates of steps S2 and S3: mechanistically, however, this competition stems from a balance between the vacancy diffusion and the surface diffusion of the charged oxygen adatom. The GDC conductivity maintains a dominant role among the transport routes, while the LSCF vacancy diffusion has no impact. Notably, clear Gerischer-like shapes are still observed in the arcs (Fig. 3c and 3d), although the lattice diffusion in the MIEC phase does not limit the performance. The kinetic picture maintains substantially unaltered also in the case polarization is applied to the electrode (not reported): the sensitivity analysis confirms that the TPB pathway governs the kinetics, consistently with the results of Ref. [33]. Nonetheless, the importance of the first electronation step S2 progressively grows compared to step S5 of electronation at the TPB, evidencing a more influential role of the LSCF surface.

With respect to the impact of the morphologic parameters, the same considerations proposed at 700°C hold at lower temperatures, as a consequence of the fact that the RDS depends on the TPB length. Finally, no effect on R_{Pol} is found in the case of the GDC/LSCF interface capacitance, which exclusively influences the shape of the imaginary part of the spectra. Instead, the surface capacitance shows an effect, due to the fact that it contributes to the surface overpotential $\Delta\chi$, which adds to the

bulk overpotential η. However, even if the equilibrium overpotential χ^{eq} is relevant (Table 5), this effect is limited and mostly complementary to that of the second electronation rate (S3).

5. Discussion

Different models are proposed in the literature to describe the ORR in composite cathodes with a MIEC electrodic phase and a purely ionic conductive electrolyte. It is then important to highlight the features that distinguish the present approach from those already published.

Heterogeneous modeling approach. The main novelty of the model lies in the individual description of the ionic conductive phase and of the MIEC phase, according to a strictly heterogeneous description of the porous electrode. Aside of the material balance of molecular O_2, one charge balance is written for the GDC phase, which entails the conduction of oxide ions, and two balances are considered for the semiconducting LSCF phase, which take into account the transport of oxide ions and electrons, respectively. Differently, the models presented by Yurkiv et al. [10] and by Mortensen et al. [31, 32] assume a pseudo-homogenous approach in the description of the composite electrode, which includes only one charge transport equation for the oxide ions within a single phase: this phase consists of a mixture of the electrolyte material and of the MIEC material, whose conduction properties are taken as an average, weighted on the volumetric fractions (Eq. 47, from Ref. [10]). As a consequence, an electroneutral pseudo-vacancy species ($V_{\ddot{o},E} + 2e^-$) is considered and the chemical potential of the vacancies in the ionic conductive phase is equilibrated with that of the MIEC phase. Additionally, the electronic conductivity of the semiconducting phase is neglected, being much higher than the average ionic

conductivity. The Faradic current density is then referred to the ionic potential, and no specification on the dependencies from the species concentration can be provided.

$$C_{DL}^{int} \cdot a_v^{int} \cdot \frac{d\Delta\phi}{dt} = \left(\frac{\varepsilon_E}{\tau_E} \cdot \sigma_{ion,E} + \frac{\varepsilon_M}{\tau_M} \cdot \sigma_{ion,M}\right) \cdot \frac{d^2\Delta\phi}{dz^2} - \hat{I}_F \qquad (47)$$

The distinction between the MIEC phase and the ionic phase has been previously adopted by Banerjee and Deutschmann [27] for LSM-YSZ cathodes, although the description of the individual reactive species is not taken into account, in order to limit the number of unknown fitting parameters. Laurencin and coworkers [14] include detailed material balances of the reacting species, but treat exclusively the steady state form and an isothermal case: the model is validated based on the polarization resistance of pure LSCF cathodes at a fixed temperature, therefore neither pre-exponential factors nor activation energies are provided.

Kinetic effect of O_2 partial pressure. The vast majority of the papers dedicated to detailed kinetic modeling of the ORR exclusively focuses on experiments performed in air, both in the case of LSCF-GDC composites [6, 10, 14] and of LSM-YSZ composites [27]. Only exceptionally a cathode is exposed to under-oxygenated atmospheres, owing to the fact that SOFCs are typically operated under large excess of air with limited conversion of O_2. Nonetheless, investigating the composite's behavior at varying O_2 partial pressure allows to refine the kinetic scheme and check the presence of diffusive limitations. The scheme proposed in this work predicts the variation of O_2 between 5% and 21% molar fraction that occurs under a defined amount of time (hour-basis) and according to slow and gradual changes. It is indeed important to recall that, when O_2 was varied, the electrode's activity experienced a modification and the measurements were taken only after stabilization of the signal, typically within one hour. This indicates that rapid variations of the O_2 partial pressure lead to different effects, with smaller polarization resistances.

5.1 Steady state behavior

The analysis of the steady state behavior provides insight in the design criteria of the composite electrode. The optimal thickness, which minimizes the polarization resistance at fixed operative temperature, can be predicted. Figure 8 shows the variation of R_{Pol} as a function of the cathode thickness at varying current density, in air at 700°C. The simulations are performed considering the same morphologic properties and transport properties of the cathode analyzed experimentally (Table 1 and Table 2). All the curves show the same evolution, with a vertical asymptote, a minimum and a linear growth at increasing thickness. The optimal cathode thickness corresponds to the minimum. At OCV, the vertical asymptote is met when the cathode thickness approaches zero, while the minimum is located approximately at 10 μm. This behavior is rationalized considering that, when the electrode is too thin, the active surface area and the interfacial area limit the activity: not enough reaction sites are available for the ORR, leading to high resistance. Upon increasing the thickness, the active surface grows, finally reaching an extent that does not limit the kinetics. Upon further expanding the thickness, at OCV, the polarization resistance linearly grows, due to increased resistance to charge transport: the electrochemically active area is larger, but also the distance travelled by oxide ions increases. In these conditions, the O_2 consumption is null and concentration polarization plays a negligible role. When current is supplied to the electrode, two main features are evident: the high polarization limit shifts to higher electrode thickness, and the slope of the linear branch increases. Moving from 0.5 to 1 A/cm^2, the limit electrode thickness grows from 5 μm to 10 μm, while the optimal thickness increases from 12 μm to 20 μm. The limit electrode thickness becomes progressively higher since a larger surface is required to support the incoming current. When the electrode

thickness exceeds the optimal value, R_{Pol} keeps increasing due to the charge transport resistance and to the additional contribution of concentration polarization. The larger the current supplied is, the larger the concentration gradient in the electrode becomes, due to increasing O_2 consumption. In turn, the larger diffusive barrier leads to higher polarization losses. The optimal thickness is met when the limit for kinetic starvation and the contributions of transport and diffusive resistances balance.

The results of Figure 8 are in line with those simulated by Bertei et al. [67] and experimentally measured by Barbucci et al. [68] on LSM-YSZ composite cathodes at OCV between 850°C and 600°C. In the case of the predictions of Nielsen et al. [6], based on the transmission line model, the absence of gas diffusive terms and the predominant role of the GDC vacancy diffusion do not highlight the linear growth branch, and rather lead to a horizontal asymptote, suggesting only that the LSCF-GDC composites should not be too thin. Noteworthy, the present results add to the literature picture the effect of the current density: a unique optimal electrode thickness cannot be found, since the minimum shifts towards larger values the larger the supplied current is. Thicker cathode layers are then required when the cell performance asks for high current extraction, while thin electrodes can lead to excess resistance.

The model also highlights in detail to what extent the ORR penetrates from the electrode/electrolyte interface within the electrode. This characteristic length, which is influenced by the concentration perturbation, can be readily visualized. Figure 9 displays the evolution of the ionic and electronic current densities in different operating conditions, labelled with letters on the curves of Figure 8. Point A is set in correspondence of the optimal cathode thickness at OCV: in this situation, the electrode thickness perfectly matches the characteristic length and no inactive zone exists. Along the whole volume, the ionic current density is transported exclusively by

the GDC phase, while the LSCF phase works as an electrochemical source of oxide ions. When the cathode is thinner than the optimal thickness, as in point B, the length required by the ORR should be higher than the available cathode thickness. Then, not only the polarization resistance steeply grows, but part of the ionic current is transported by the LSCF phase, instead of being carried only by GDC. This is a specific and key-result of the present model, which suggests that R_{Pol} increases also due to the fact that LSCF is a poorer ionic conductor compared to GDC. As a matter of fact, a macrohomogeneous modeling approach, wherein an average ionic conductivity is defined, could not have evidenced this feature. A different situation emerges when a high current density is supplied to a thick cathode, for instance in the case of 1 A/cm^2 and 100 μm thickness (Point C). The characteristic length is completely developed, up to 20 μm, and the remaining part of the electrode just acts as a diffusive barrier, adding a distance to be covered by the ions. Interestingly, although the current is mainly carried by GDC, a small fraction (~10%) also travels in LSCF: apparently, in this case, LSCF works as a dumper and adsorbs part of the current, reducing the electrochemically active zone.

The relationship between the characteristic length and the electrode thickness at different current conditions has a well-known effect on the shape of the impedance arcs. The panels of Figure 8 illustrate this effect (in case of unitary γ_{CPE}). When the characteristic length matches the electrode thickness (point A), a Gerischer arc is found. If the electrode is too thin, a transition is observed from Gerischer arcs to arcs characterized by a $\pi/4$ high frequency branch followed by a semicircle (point B). When the electrode is much thicker than the length required by the reaction (point C), the shape of point B is retained, although it is mainly associated to diffusive limitations.

6. Conclusion

In this work, we report a physically-based model for the description of LSCF-GDC ($La_{0.4}Sr_{0.6}Co_{0.2}Fe_{0.8}O_{3-\delta}/Ce_{0.9}Gd_{0.1}O_{2-\delta}$) composite electrodes, capable of predicting impedance spectra measured during the reaction of oxygen reduction. The model is heterogeneous and dynamic, and includes a detailed multistep kinetic scheme of the ORR. A novel approach is applied, wherein the electrode structure is explicitly solved for each phase, with individual balances of mass for the LSCF vacancies and charge for GDC. A pseudo-homogenous and continuum approach, wherein the MIEC and the electrolyte phases are not distinguished, is purposely avoided, and a fully heterogeneous impedance model is proposed. The model also includes fundamental conservation equations for surface species, and treats rigorously the diffusion of O_2 in the porous electrode's matrix, as well as the estimation of the microstructural properties. Butler-Volmer rates are considered for charge-transfer reactions, which are referenced to two distinct overpotentials, the bulk overpotential for the 2PB step and the surface overpotential in the case of the electronation steps. A large pool of thermodynamic and transport properties available in the literature is accounted for, in order to guarantee consistency to the kinetic scheme and limit the number of tunable unknown parameters. The kinetic parameters are derived by fitting to experimental impedance data collected on well-characterized, inhouse-made symmetric cells mounting standard LSCF-GDC electrodes and tested between 560°C and 700°C, at OCV, with O_2/N_2 mixtures at varying O_2 content from 5% to 21%. The scheme is validated onto independent datasets taken from relevant literature [6]. The sensitivity analysis shows that the inclusion of a single-charged oxygen adatom in the GDC lattice governs the ORR mechanism and that the TPB path prevails over the 2PB path under all the examined conditions. LSCF is found to play distinct roles, depending on the electrode's polarization: LSCF primarily acts as O_2 activator,

adsorbing and charging oxygen atoms, and transfers oxide ions to the interface with GDC, which in turn acts as a rapid oxide ion vector, along the electrode up to the interface with the electrolyte. Though, when sufficient current is supplied, lattice transport within LSCF activates in parallel to the main path within GDC. The individuation on this parallel transfer mode is an original result, which only a fully heterogeneous description of the electrode can point out. The effect of the electrode's thickness is investigated in terms of polarization resistance and shape of the impedance arcs. A transition from the Gerischer shape to more complex shapes is highlighted and associated to the relationship between the electrode thickness and the penetration depth of the electrochemical reaction. A full set of revised thermodynamic and kinetic parameters is presented, which make the present model a tool to optimize the structure of applicative LSCF-GDC electrodes.

Appendix A

The electrode potential V_{eld} is defined as the difference between the electrons potential in the current collector CC and the potential of the electrolyte at the electrode/electrolyte interface (Eq. A1). In line with literature models from the porous electrode theory [49], this relationship translates a difference between the electrostatic potential of the metal backing of the porous cathode (i.e. the current collector) and the potential of the electrolyte at the pores mouth. In the present case, Equation A1 implies that the electrolyte potential right next to the interface equals that at the interface (z = End).

$$V_{eld} = \phi^{e}_{CC}|_{0} - \phi^{b}_{E}\big|_{End} \qquad \text{(A1)}$$

Equation 18 of the model is obtained assuming that the LSCF electrons are in equilibrium with the electrons of the current collector, and therefore states that the electrode potential corresponds to the difference between the GDC potential and the LSCF potential taken at the two sides of the cathode. Such definition implies that no contact resistance is accounted for between the current collector and the electrode, and that the electrochemical potential of the electrons is uniform across the interface. In line with relevant literature works [27, 28, 38, 69], the ohmic resistance of the electrolyte is not included, and the counter electrode is taken as a perfect electrode with null overpotential. As a matter of fact, the equation for the electrode potential describes a situation wherein a reference electrode is located right in proximity of the electrode/electrolyte interface. Setting the potential of the LSCF phase as zero at the current collector, the electrode potential is calculated.

$$V_{eld} = \phi^{b}_{M}\big|_{0} - \phi^{b}_{E}\big|_{End} \qquad \text{(18)}$$

Better insight into the meaning of equation 18 is obtained by substitution of equation 19 of the bulk overpotential and rearrangement of the equilibrium potential $\Delta\phi^{eq}$ associated to reaction S4.

$$V_{eld} = \left(\phi_M^b\big|_0 - \phi_M^b\big|_{End}\right) + \left(\phi_M^b\big|_{End} - \phi_E^b\big|_{End}\right) \quad \text{(A2)}$$

$$V_{eld} = \eta|_{End} + \frac{RT}{2F}\cdot ln\left(\frac{C_{V_{\ddot{O}},M}^{eq}\cdot C_{O_{o,E}^x}^{eq}}{C_{O_{o,M}^x}^{eq}\cdot C_{V_{\ddot{O}},M}^{eq}}\cdot\frac{C_{V_{\ddot{O}},E}\cdot C_{O_{o,M}^x}}{C_{V_{\ddot{O}},M}\cdot C_{O_{o,E}^x}}\right) + \left(\phi_M^b\big|_0 - \phi_M^b\big|_{End}\right) \quad \text{(A3)}$$

The resulting equation (Eq. A4) is obtained by noting that the electrolyte species are invariant and equilibrated (assumption 6). It evidences that the electrode potential is the sum of three main contributions: the bulk overpotential at the electrode/electrolyte interface, which is the maximum value reached within the cathode volume; the equilibrium potential difference, which mirrors the concentration overpotential of vacancies and oxide ions in the LSCF lattice; a term due to gradient of the electrical potential in LSCF, which arises by the consideration of electrons transport in the model (Eq. 15).

$$V_{eld} = \eta|_{End} + \frac{RT}{2F}\cdot ln\left(\frac{C_{O_{o,M}^x}}{C_{V_{\ddot{O}},M}}\cdot\frac{C_{V_{\ddot{O}},M}^{eq}}{C_{O_{o,M}^x}^{eq}}\right)\Bigg|_{End} + \left(\phi_M^b\big|_0 - \phi_M^b\big|_{End}\right) \quad \text{(A4)}$$

It is worthy to note that this form of the electrode potential is consistent with that provided in Ref. [27] and [69], which is equal to the applied overpotential, given that the LSCF potential is found to be almost gradient-less and the deviation of the vacancies and oxide ions from the equilibrium values is limited. Additionally, it can be demonstrated that the contribution associated to the electron transport is equal to that found by Jin et al. [42] when rigorously deriving the potential of MIEC electrodes.

Appendix B

Key saving of computational time, which allows to apply the regression routine, is achieved by transformation of the DAE system into an algebraic complex system of oscillating variables. Full details on the method are found in Ref. [63]. In this appendix, the main model equations described in Section 3.2 are presented in the oscillating form. The oscillating part of each variable is represented by a tilde, the steady state part is represented by an overbar, and *j* is the imaginary unit. The equations reported are the result of the transformation. The material balance on molecular oxygen O_2 (Eq.1) and the definition of its diffusive molecular flux (Eq. 3) are written as:

$$\varepsilon \cdot j\omega \cdot \tilde{C}_{O_2} = -\frac{d\tilde{J}_{O_2}}{dz} - a_v^{ads} \cdot \tilde{r}_1 \qquad \text{(B1)}$$

$$\tilde{J}_{O_2} = -D_{O_2}^{eff} \cdot \frac{d\tilde{C}_{O_2}}{dz} \qquad \text{(B2)}$$

The oscillating form of the kinetic rate r_1 (Eq. 31) is given by:

$$\tilde{r}_1 = 2 \cdot \vec{k}_1 \cdot \Gamma^2 \cdot \bar{\theta}_F \cdot \bar{P}_{O_2} \cdot \tilde{\theta}_F + \vec{k}_1 \cdot \Gamma^2 \cdot \bar{\theta}_F^2 \cdot \tilde{P}_{O_2} - 2 \cdot \overleftarrow{k}_1 \cdot \Gamma^2 \cdot \bar{\theta}_{O_M^{ads}} \cdot \tilde{\theta}_{O_M^{ads}} \qquad \text{(B3)}$$

The conservation equations of the surface species (Eq. 4 to 6) lead to the following complex forms:

$$j\omega \cdot a_v^{ads} \cdot \Gamma \cdot \tilde{\theta}_{O_M^{ads}} = a_v^{ads} \cdot (2 \cdot \tilde{r}_1 - \tilde{r}_2) \qquad \text{(B4)}$$

$$j\omega \cdot a_v^{ads} \cdot \Gamma \cdot \tilde{\theta}_{O_M^{-ads}} = a_v^{ads} \cdot (\tilde{r}_2 - \tilde{r}_3) - \lambda_{TPB} \cdot \tilde{r}_5 \qquad \text{(B5)}$$

$$\tilde{\theta}_F + \tilde{\theta}_{O_M^{ads}} + \tilde{\theta}_{O_M^{-ads}} = 0 \qquad \text{(B6)}$$

The reaction rates of steps S2, S3 and S5 of the mechanism (Eq. 32, 33 and to 35) give rise to quite complicated relations, due to the presence of multiple dependencies

and to the intrinsic Butler-Volmer structure. In the transformation, the equilibrium variables are taken as constant, and the equations are written considering that 1-α is equal to α (i.e. α = 0.5).

$$\tilde{r}_2 = \vec{k}_2 \cdot \Gamma \cdot \theta_{O_M^{ads}}^{eq} \cdot exp\left(-\frac{\alpha \cdot n_{e^-} \cdot F \cdot \chi^{eq}}{RT}\right) \cdot$$

$$\cdot \left\{ \frac{\tilde{\theta}_{O_M^{ads}}}{\theta_{O_M^{ads}}^{eq}} \cdot exp\left(-\frac{\alpha \cdot n_{e^-} \cdot \mathrm{F} \cdot \Delta\bar{\chi}}{RT}\right) - \frac{\tilde{\theta}_{O_M^{-ads}}}{\theta_{O_M^{-ads}}^{eq}} \cdot exp\left(+\frac{\alpha \cdot n_{e^-} \cdot \mathrm{F} \cdot \Delta\bar{\chi}}{RT}\right) - \frac{\alpha \cdot n_{e^-} \cdot \mathrm{F}}{RT} \cdot \tilde{\chi} \right.$$

$$\left. \cdot \left[\frac{\bar{\theta}_{O_M^{ads}}}{\theta_{O_M^{ads}}^{eq}} \cdot exp\left(-\frac{\alpha \cdot n_{e^-} \cdot \mathrm{F} \cdot \Delta\bar{\chi}}{RT}\right) + \frac{\bar{\theta}_{O_M^{-ads}}}{\theta_{O_M^{-ads}}^{eq}} \cdot exp\left(\frac{\alpha \cdot n_{e^-} \cdot \mathrm{F} \cdot \Delta\bar{\chi}}{RT}\right) \right] \right\}$$

(B7)

$$\tilde{r}_3 = \vec{k}_3 \cdot \Gamma \cdot \theta_{O_M^{-ads}}^{eq} \cdot C_{V_{\ddot{o},M}}^{eq} \cdot exp\left(+\frac{\alpha \cdot n_{e^-} \cdot F \cdot \chi^{eq}}{RT}\right) \cdot$$

$$\cdot \left\{ \left(\frac{\tilde{C}_{V_{\ddot{o},M}}}{C_{V_{\ddot{o},M}}^{eq}} \cdot \frac{\bar{\theta}_{O_M^{-ads}}}{\theta_{O_M^{-ads}}^{eq}} + \frac{\bar{C}_{V_{\ddot{o},M}}}{C_{V_{\ddot{o},M}}^{eq}} \cdot \frac{\tilde{\theta}_{O_M^{-ads}}}{\theta_{O_M^{-ads}}^{eq}} \right) \cdot exp\left(+\frac{\alpha \cdot n_{e^-} \cdot \mathrm{F} \cdot \Delta\bar{\chi}}{RT}\right) \right.$$

$$- \left(\frac{\tilde{\theta}_F}{\theta_F^{eq}} \cdot \frac{\bar{C}_{O_{o,M}^x}}{C_{O_{o,M}^x}^{eq}} + \frac{\bar{\theta}_F}{\theta_F^{eq}} \cdot \frac{\tilde{C}_{O_{o,M}^x}}{C_{O_{o,M}^x}^{eq}} \right) \cdot exp\left(-\frac{\alpha \cdot n_{e^-} \cdot \mathrm{F} \cdot \Delta\bar{\chi}}{RT}\right)$$

$$+ \left[\frac{\bar{C}_{V_{\ddot{o},M}}}{C_{V_{\ddot{o},M}}^{eq}} \cdot \frac{\bar{\theta}_{O_M^{-ads}}}{\theta_{O_M^{-ads}}^{eq}} \cdot exp\left(+\frac{\alpha \cdot n_{e^-} \cdot \mathrm{F} \cdot \Delta\bar{\chi}}{RT}\right) + \frac{\bar{\theta}_F}{\theta_F^{eq}} \cdot \frac{\bar{C}_{O_{o,M}^x}}{C_{O_{o,M}^x}^{eq}} \right.$$

$$\left. \left. \cdot exp\left(-\frac{\alpha \cdot n_{e^-} \cdot \mathrm{F} \cdot \Delta\bar{\chi}}{RT}\right) \right] \cdot \frac{\alpha \cdot n_{e^-} \cdot \mathrm{F}}{RT} \cdot \tilde{\chi} \right\}$$

(B8)

$$\tilde{r}_5 = \vec{k}_5 \cdot \Gamma \cdot \theta_{O_M^{-ads}}^{eq} \cdot C_{V_{\ddot{o},E}}^{eq} \cdot exp\left(-\frac{\alpha \cdot n_{e^-} \cdot F \cdot \Delta\phi_{TPB}^{eq}}{RT}\right) \cdot$$

$$\cdot\left\{\frac{\tilde{\theta}_{O_M^{-ads}}}{\theta_{O_M^{-ads}}^{eq}}\cdot exp\left(-\frac{\alpha\cdot n_{e^-}\cdot F\cdot\bar{\eta}_{TPB}}{RT}\right)-\frac{\tilde{\theta}_F}{\theta_F^{eq}}\cdot exp\left(+\frac{\alpha\cdot n_{e^-}\cdot F\cdot\bar{\eta}_{TPB}}{RT}\right)\right.$$

$$-\left[\frac{\bar{\theta}_{O_M^{-ads}}}{\theta_{O_M^{-ads}}^{eq}}\cdot exp\left(-\frac{\alpha\cdot n_{e^-}\cdot F\cdot\bar{\eta}_{TPB}}{RT}\right)+\frac{\bar{\theta}_F}{\theta_F^{eq}}\right.$$

$$\left.\left.\cdot exp\left(+\frac{\alpha\cdot n_{e^-}\cdot F\cdot\bar{\eta}_{TPB}}{RT}\right)\right]\cdot\frac{\alpha\cdot n_{e^-}\cdot F}{RT}\cdot\tilde{\eta}_{TPB}\right\}$$

(B9)

After the transformation, the charge conservation equations for the two phases (Eq. 7), the definitions of the oxide ion fluxes (Eq. 8) and of the ionic potentials (Eq. 12) become:

$$(1-\varepsilon)\cdot f_M\cdot j\omega\cdot\tilde{C}_{V_{\ddot{o},M}}=-\frac{d\tilde{J}_{V_{\ddot{o},M}}}{dz}-a_v^{ads}\cdot\tilde{r}_3+a_v^{int}\cdot\tilde{r}_4 \qquad \text{(B10)}$$

$$\tilde{J}_{V_{\ddot{o},M}}=-A\cdot D_{V_{\ddot{o},M}}^{eff}\cdot\frac{d\tilde{C}_{V_{\ddot{o},M}}}{dz}-\frac{z_{V_{\ddot{o}}}F\cdot A\cdot D_{V_{\ddot{o},M}}^{eff}}{RT}\cdot\tilde{C}_{V_{\ddot{o},M}}\cdot\frac{d\tilde{\phi}_M^b}{dz} \qquad \text{(B11)}$$

$$j\omega\cdot C_{DL}^{int}\cdot a_v^{int}\cdot\tilde{\eta}=\sigma_{ion,E}^{eff}\cdot\frac{d^2\tilde{\phi}_E^b}{dz^2}-n_{V_{\ddot{O}}}\cdot F\cdot\left(a_v^{int}\cdot\tilde{r}_4+\lambda_{TPB}\cdot\tilde{r}_5\right) \qquad \text{(B12)}$$

The oscillating form of the rate of the ionic transport across the LSCF/GDC interface (S4) is written as:

$$\tilde{r}_4=\vec{k}_4\cdot C_{O_{o,M}^x}^{eq}\cdot C_{V_{\ddot{O}},E}^{eq}\cdot exp\left(-\frac{\alpha\cdot n_{V_{\ddot{O}}}\cdot F\cdot\Delta\phi^{eq}}{RT}\right)\cdot\left\{\frac{\tilde{C}_{O_{o,M}^x}}{C_{O_{o,M}^x}^{eq}}\cdot exp\left(-\frac{\alpha\cdot n_{V_{\ddot{O}}}\cdot F\cdot\bar{\eta}}{RT}\right)-\frac{\tilde{C}_{V_{\ddot{o},M}}}{C_{V_{\ddot{O}},M}^{eq}}\cdot\right.$$

$$\left.exp\left(+\frac{\alpha\cdot n_{V_{\ddot{O}}}\cdot F\cdot\bar{\eta}}{RT}\right)-\left[\frac{\bar{C}_{O_{o,M}^x}}{C_{O_{o,M}^x}^{eq}}\cdot exp\left(-\frac{\alpha\cdot n_{V_{\ddot{O}}}\cdot F\cdot\bar{\eta}}{RT}\right)+\frac{\bar{C}_{V_{\ddot{o},M}}}{C_{V_{\ddot{O}},M}^{eq}}\cdot exp\left(+\frac{\alpha\cdot n_{V_{\ddot{O}}}\cdot F\cdot\bar{\eta}}{RT}\right)\right]\cdot\frac{\alpha\cdot n_{V_{\ddot{O}}}\cdot F}{RT}\cdot\tilde{\eta}\right\}$$

(B13)

The description of the oxide ion conduction in LSCF is completed by the conservation of oxide oxygen sites (Eq. B14). The transference of electronic current in the

electrode is described by the Ohm's law (Eq. 15) and by the conservation of current density (Eq. 16). In this latter equation, the transformation leads to the appearance of the perturbed current amplitude $\tilde{I}_P$, which is the driving force of the measurements.

$$\tilde{C}_{V_{\ddot{o},M}} + \tilde{C}_{O^x_{o,M}} = 0 \qquad \text{(B14)}$$

$$z_{V_{\ddot{o}}} \cdot F \cdot \left(\tilde{J}_{V_{\ddot{o},E}} + \tilde{J}_{V_{\ddot{o},M}}\right) + \tilde{I}^E_{ion} = \tilde{I}_P \qquad \text{(B15)}$$

$$\tilde{I}_{e-} = -\sigma^{eff}_{el,M} \cdot \frac{d\tilde{\phi}^b_M}{dz} \qquad \text{(B16)}$$

Finally, the system equations are completed by the set related to the definitions of potentials and overpotentials (Eq. 18 to Eq. 24), and by the boundary conditions (Eq. 25 to Eq. 30). The oscillating forms of the first set of equations are presented below, noting that the equilibrium potential is assumed constant and non-oscillating.

$$\tilde{\eta} = \tilde{\phi}^b_M - \tilde{\phi}^b_E \qquad \text{(B17)}$$

$$\Delta\tilde{\chi} = \frac{\Gamma \cdot F}{C^{surf}_{DL}} \cdot \tilde{\theta}_{O^{-ads}_M} \qquad \text{(B18)}$$

$$\tilde{\eta}_{TPB} = 2\tilde{\eta} - \Delta\tilde{\chi} \qquad \text{(B19)}$$

$$\tilde{V}_{eld} = \tilde{\phi}^b_M\big|_0 - \tilde{\phi}^b_E\big|_{End} \qquad \text{(B20)}$$

The boundary conditions at the current collector (z = 0) entail the CSTR-type continuity equation on the molar flow rates, the assumptions on MIEC and electrolyte potentials, as well as the no-flux condition for the vacancies of the MIEC.

$$j\omega \cdot V_{CSTR} \cdot \tilde{C}_i\big|_0 = -F^{Out}_{tot} \cdot \frac{\tilde{C}_i|_0}{\bar{C}_{tot}|_0} + S_{el} \cdot \left[\sum_{i=1}^{NS}\left(\frac{\bar{J}_i}{\bar{C}_{tot}|_0} \cdot \tilde{C}_i\big|_0 + \bar{y}_i|_0 \cdot \tilde{J}_i\big|_0\right) - \tilde{J}_i\big|_0\right] \qquad \text{(B21)}$$

$$\tilde{\phi}^b_M\big|_0 = \tilde{\phi}^b_E\big|_0 = 0 \qquad \text{(B22)}$$

$$\tilde{J}_{V_{\ddot{o},M}}\big|_0 = 0 \qquad \text{(B23)}$$

$$\left.\frac{d\tilde{C}_{V_{\ddot{o},M}}}{dz}\right|_0 = 0 \qquad \text{(B24)}$$

One boundary condition is set at the electrode/electrolyte interface (z = End). It defines the local potential of the electrolyte phase, by establishing that the electronic current applied to the electrode at the current collectors enters the solid electrolyte through the GDC and the LSCF phase (B24).

$$-\sigma_{ion,E}^{eff} \cdot \left.\frac{d\tilde{\phi}_E^b}{dz}\right|_{End} + z_{V_{\ddot{o}}} \cdot F \cdot \tilde{J}_{V_{\ddot{o},M}}\big|_{End} = \tilde{I}_P \qquad \text{(B24)}$$

Tables

Table 1: morphologic parameters used in the simulations. The values reported for the specific interfacial area, the specific adsorption area, the TPB length per unit volume and the pore size are calculated according to the percolation theory. f_{LSCF} and f_{GDC} are the volume fractions of GDC and LSCF particles in the LSCF-GDC mixture. $Z_{LSCF,LSCF}$ and $Z_{GDC,GDC}$ are the contact numbers, calculated according to the correlations provided by Chen et al. [47].

Parameter	Value
Thickness	70 μm
Porosity	0.40
Tortuosity	2.8
Cell diameter	1.1 cm
LSCF particle size	0.8 μm
GDC particle size	0.8 μm
Pore size	0.3 μm
a_V^{int}	9.41×10^{4} m^2 m^{-3}
a_V^{ads}	2.38×10^{6} m^2 m^{-3}
λ_{TPB}	1.81×10^{12} m m^{-3}
Γ	1.1×10^{-5} mol m^{-2}
f_{LSCF}	0.53
f_{GDC}	0.47
$Z_{LSCF,LSCF}$	3.18
$Z_{GDC,GDC}$	2.82

Table 2: capacitive and transport parameters used in the simulations.

Parameter	Value	Source
C_{DL}^{int}	$2.3\times10^{11}\times\exp(-146\times10^{3}/R/T)$ F m^{-2}	Fit
γ_{CPE}	0.90	Fit
C_{DL}^{surf}	0.1 F m^{-2}	[36]
σ_{GDC}^{ion}	$1.25\times10^{5}/T\times\exp(-69.7\times10^{3}/R/T)$ S cm^{-1}	EIS
σ_{LSCF}^{ele}	$-0.627\times T+983.25$ S cm^{-1} (T > 923 K)	[66]
$D_{V_{ö,M}}^{\delta}$	$5.8\times10^{-4}\times\exp(-121\times10^{3}/R/T)$ cm^2 s^{-1}	[21]
A	$1.9696\times\exp(+38.77\times10^{3}/R/T)$	[12]

Table 3: kinetic parameters used in the numerical simulations. The values are calculated by fitting to the data reported in Figure 3.

Reaction Step	$\vec{k}$	E_{Act} [kJ/mol]
r_1	1.1×10^{10} m^2 mol^{-1} s^{-1} atm^{-1}	21.0
r_2	5.9×10^{14} s^{-1}	196.0
r_3	1.2×10^{13} m^3 mol^{-1} s^{-1}	185.9
r_4	1.8×10^{2} m^5 mol^{-1} s^{-1}	106.1
r_5	1.2×10^{5} m^4 mol^{-1} s^{-1}	148.2

Table 4: thermodynamic parameters used in the simulations. The formation enthalpies are referenced to 298 K and 1 atm, the standard entropies are referenced to 0 K and 1 atm. The values reported are calculated at 700°C.

Species	$\Delta H_i^{0,F}$ [kJ/mol]	S_i^0 [J/mol/K]	Source
O_2	21.8	242.6	[52]
O_M^{ads}	-83.2	0	[57]
O_M^{-ads}	-88.4	0	[10]
\$	0	0	[10]
$V_{ö,M}$	0	0	[53]
$O_{o,M}^{x}$	-139.6	55.6	[53]
$V_{ö,E}$	0	0	[56]
$O_{o,E}^{x}$	-200.0	70.0	[56]

Table 5: surface coverage fractions predicted at the equilibrium. In equations 38 and 39 the surface equilibrium potential is calculated as $\chi^{eq} = \frac{\Gamma \cdot F}{C_{DL}^{surf}} \cdot \theta_{O_M^- ads}^{eq}$.

	P O_2 = 0.21 atm			**P O_2 = 0.10 atm**			**P O_2 = 0.05 atm**		
T [°C]	**O**	**O-**	**χ^{eq} [mV]**	**O**	**O-**	**χ^{eq} [mV]**	**O**	**O-**	**χ^{eq} [mV]**
700	4.3%	0.8%	85	3.2%	0.7%	71	2.1%	0.6%	58
650	8.0%	1.0%	106	5.7%	0.9%	93	4.1%	0.8%	80
600	15.4%	1.3%	138	11.2%	1.1%	117	8.2%	1.0%	105
560	25.9%	1.4%	149	19.5%	1.3%	138	14.6%	1.1%	117

Table 6: correlation matrix of the fitted parameters. The top arrows indicate that the parameter refers to the rate of the direct reaction step. The number indicates the step in the ORR mechanism. C_{DL}^0 and E_{Act}^{DL} are the pre-exponential factor and the activation energy of the double layer interfacial capacitance. γ is the exponent of the CPE element.

	$\vec{k}_2$	$\vec{k}_3$	$\vec{k}_1$	$\vec{k}_4$	$\vec{k}_5$	$\vec{E}_{Act}^1$	$\vec{E}_{Act}^2$	$\vec{E}_{Act}^3$	$\vec{E}_{Act}^4$	$\vec{E}_{Act}^5$	C_{DL}^0	E_{Act}^{DL}	γ
$\vec{k}_2$	1												
$\vec{k}_3$	0.37	1											
$\vec{k}_1$	-0.38	-0.68	1										
$\vec{k}_4$	0.21	-0.09	-0.17	1									
$\vec{k}_5$	-0.47	-0.48	0.39	0.09	1								
$\vec{E}_{Act}^1$	-0.09	-0.02	0.10	-0.33	-0.04	1							
$\vec{E}_{Act}^2$	0.01	0.07	-0.08	-0.24	0.12	-0.59	1						
$\vec{E}_{Act}^3$	0.06	0.02	-0.11	0.24	0.10	-0.74	0.44	1					
$\vec{E}_{Act}^4$	-0.29	-0.07	-0.03	-0.14	0.08	-0.20	-0.15	-0.16	1				
$\vec{E}_{Act}^5$	0.01	-0.16	0.11	0.40	0.23	0.49	-0.74	-0.71	0.12	1			
C_{DL}^0	0.16	-0.15	-0.16	0.25	0.18	-0.11	0.08	0.03	-0.44	0.06	1		
E_{Act}^{DL}	0.16	-0.06	-0.17	0.65	0.08	-0.26	-0.07	0.18	-0.47	0.19	0.28	1	
γ	-0.15	0.16	0.16	-0.31	-0.20	0.13	-0.06	-0.05	0.42	-0.10	-0.99	-0.30	1

Table 7: structural and transport parameters used in the simulations of the experiments by Nielsen et al. [6] reported in Figure 6.

Parameter	Value
Thickness	12 μm
Porosity	0.40
Tortuosity	2.5
Pore size	0.5 μm
a_V^{int}	7.41×10^{4} m^3 m^{-2}
a_V^{ads}	1.87×10^{6} m^3 m^{-2}
λ_{TPB}	1.43×10^{12} m m^{-3}
σ_{GDC}^{ion}	$1.09\times10^{5}/T\times\exp(-62\times10^{3}/R/T)$ S cm^{-1}

Figures

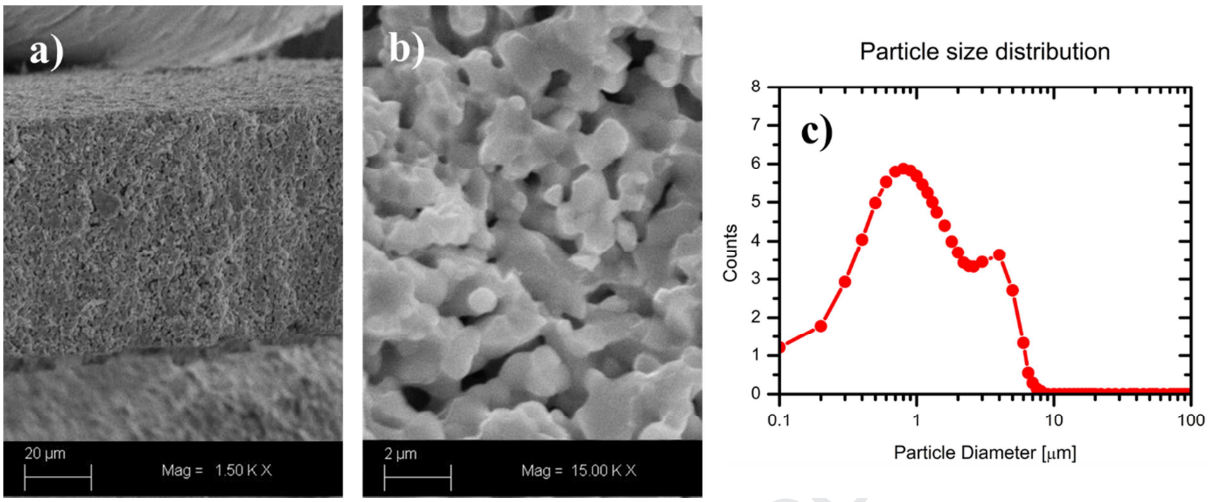

Figure 1

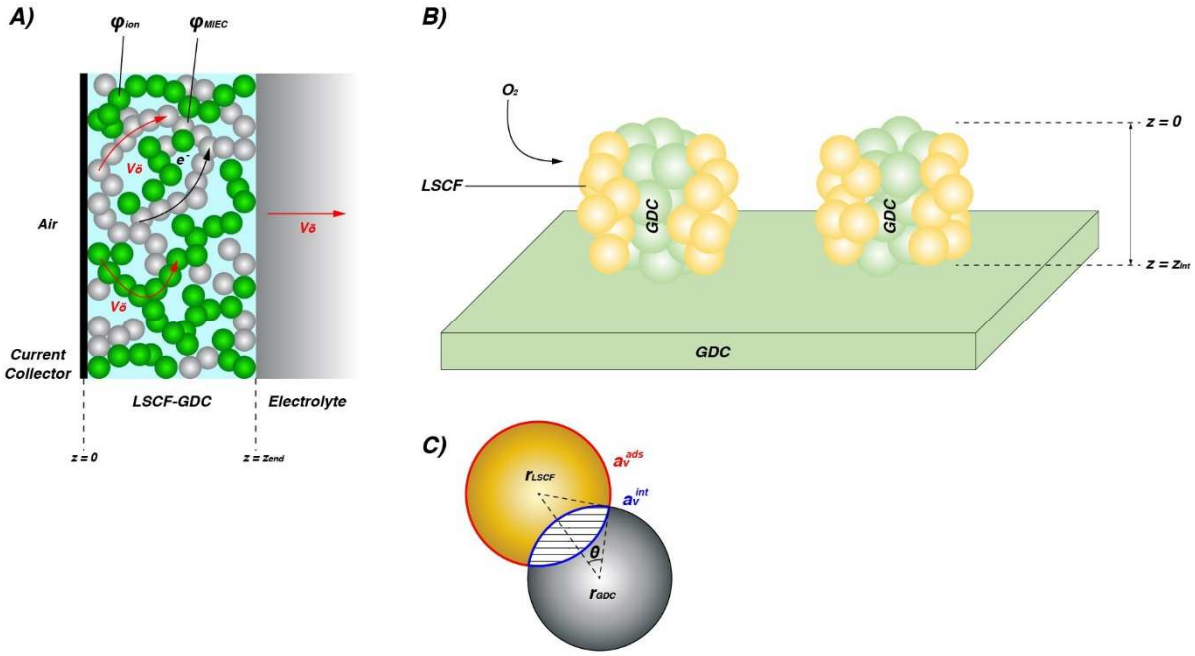

Figure 2

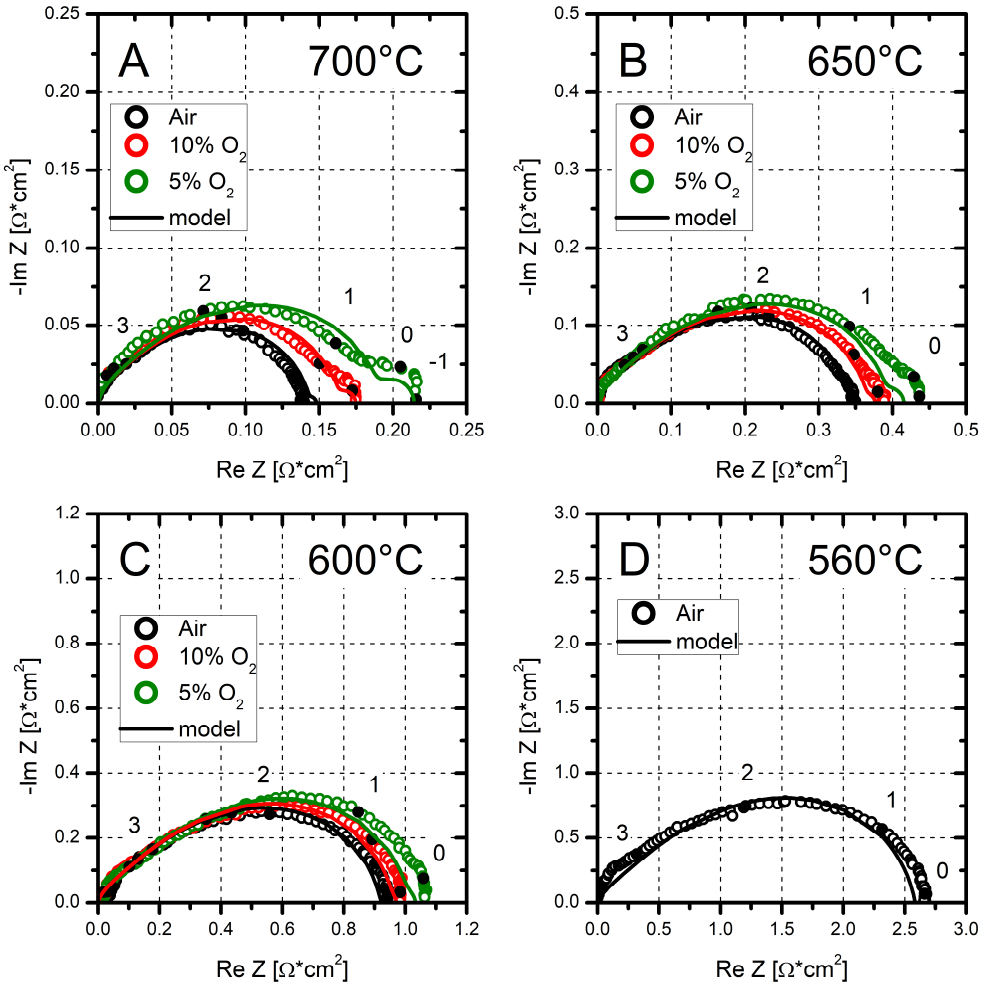
A
700°C
B
650°C
C
600°C
D
560°C
Air
10% O2
5% O2
model
-Im Z [Ω*cm2]
Re Z [Ω*cm2]
0
1
2
3
-1

Figure 3

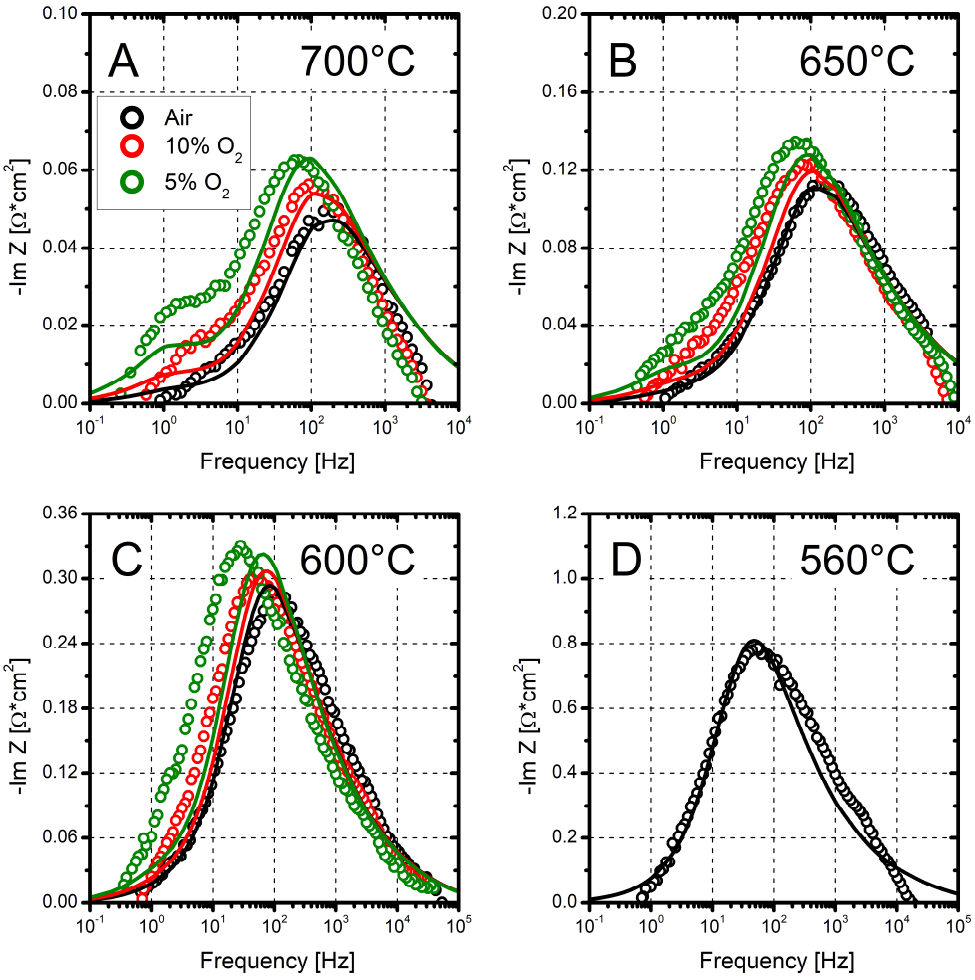

Figure 4

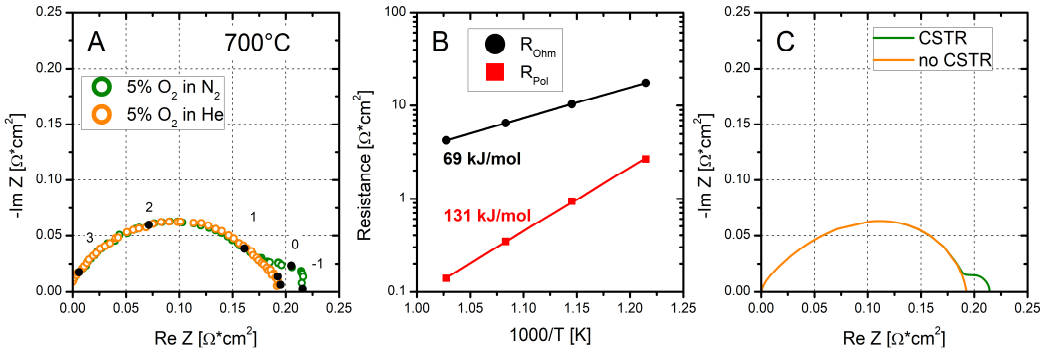
A
700°C
5% O2 in N2
5% O2 in He
-Im Z [Ω*cm2]
Re Z [Ω*cm2]
B
ROhm
RPol
69 kJ/mol
131 kJ/mol
Resistance [Ω*cm2]
1000/T [K]
C
CSTR
no CSTR
-Im Z [Ω*cm2]
Re Z [Ω*cm2]

Figure 5

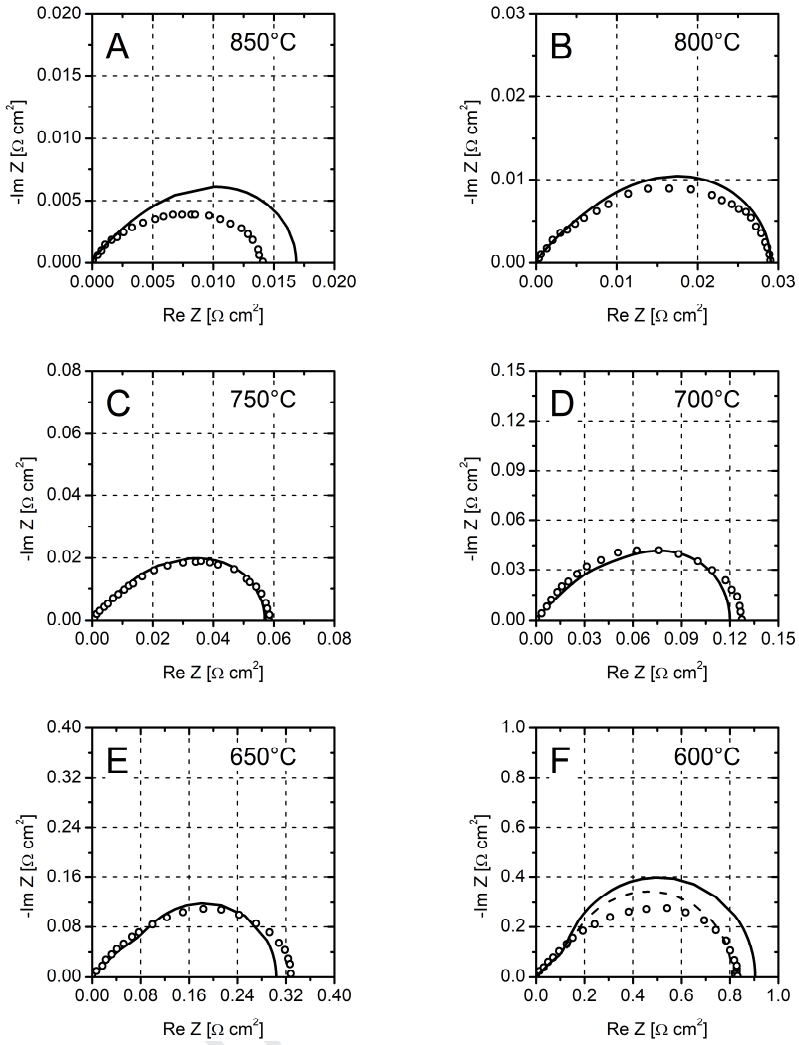

Figure 6

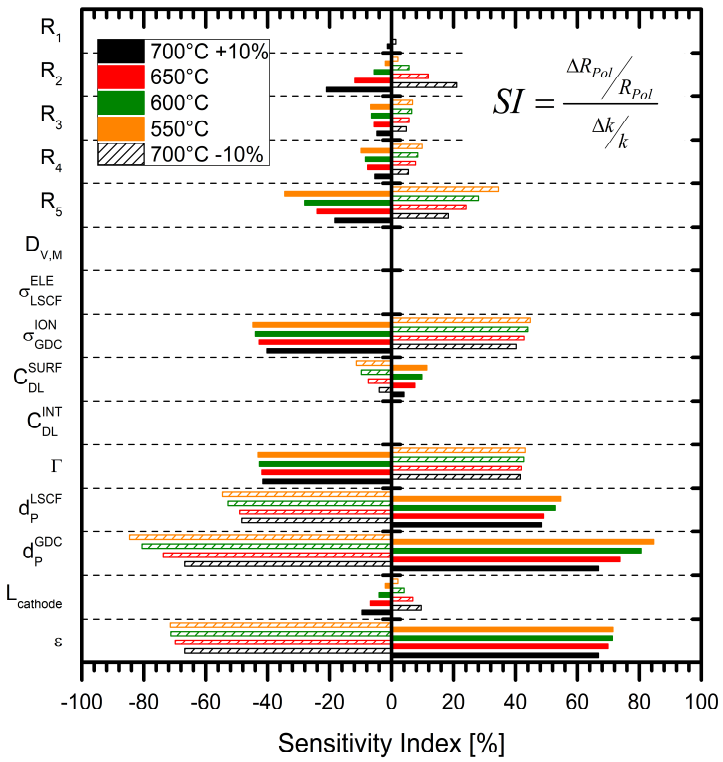

Figure 7

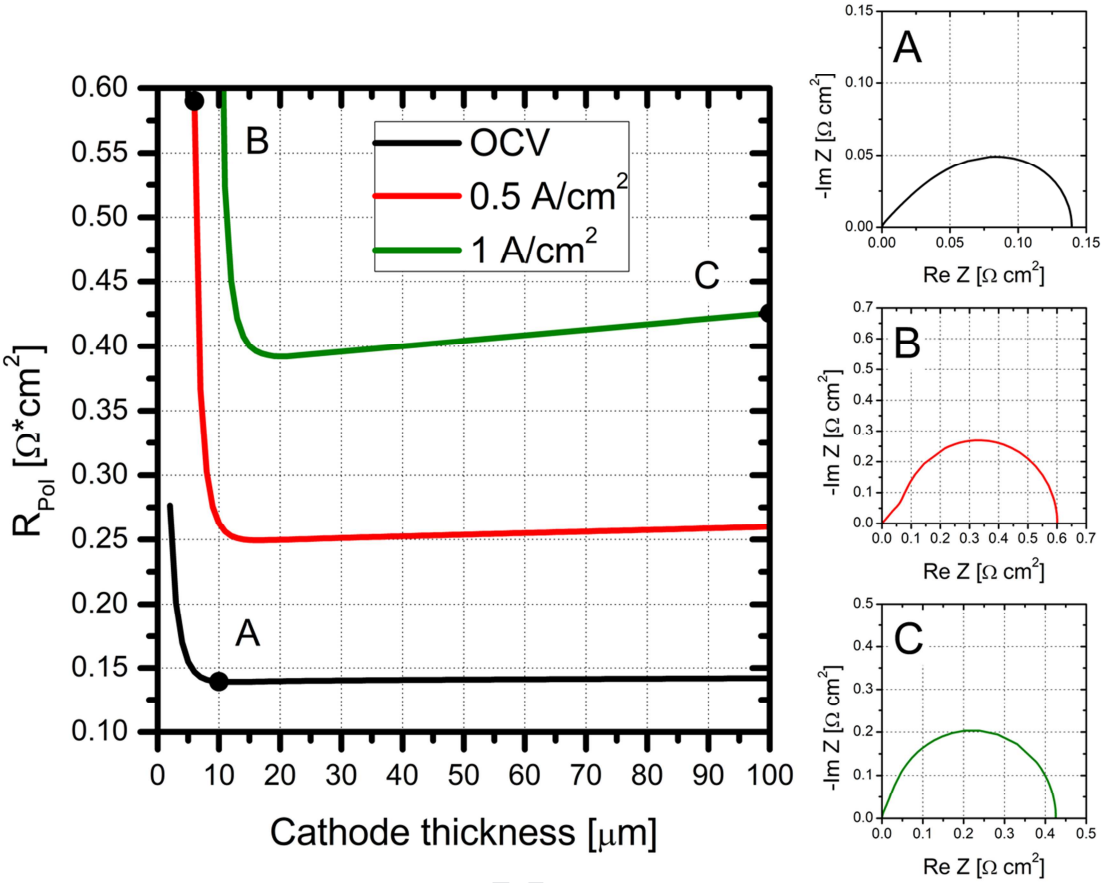

Figure 8

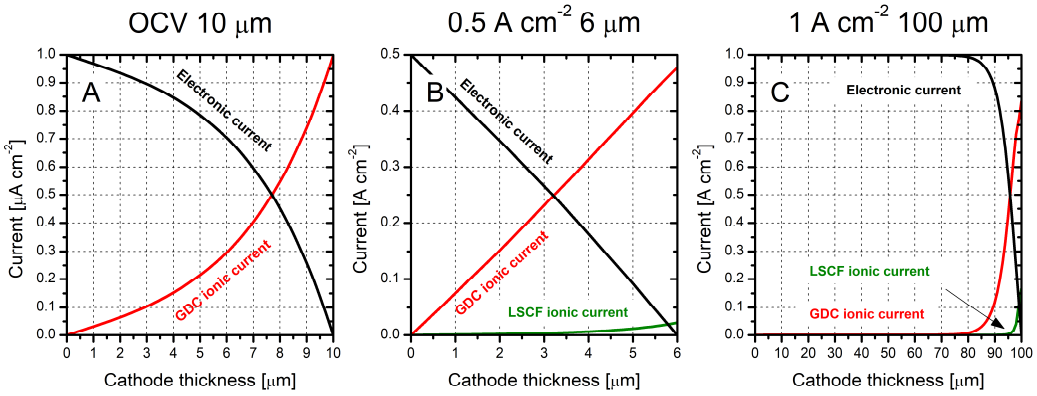
OCV 10 μm
0.5 A cm-2 6 μm
1 A cm-2 100 μm
A
B
C
Electronic current
GDC ionic current
LSCF ionic current
Current [μA cm-2]
Current [A cm-2]
Cathode thickness [μm]

Figure 9

Figure Captions

Figure 1 – SEM micrographs of the cathode section (panel A) and of the particle size (panel B). Particle size distribution as resulting from granulometry tests on the precursor ink of the composite cathode (panel C).

Figure 2 – A) sketch of the model domain. B) Detail representation of the LSCF-GDC particles and electrode as treated by the model. A zoom on percolated particles is displayed. C) Definition of the particles morphology and active surfaces. The external surface of the LSCF particles corresponds to a_V^{ads}. The interfacial section between the LSCF and the GDC particle is taken as a_V^{int}. The highlighted perimeter displays the TPB length λ_{TPB}.

Figure 3 – Model analysis of the impedance spectra measured on LSCF-GDC/GDC/LSCF-GDC symmetric cells. Operating conditions: open circuit voltage, 10 mV, 10 kHz – 10 mHz, T = 560°C – 700°C, P O_2 = 5% – 21%. Symbols are data points, line is model fittings. The logarithm of the frequency decade is indicated.

Figure 4 – Comparison between experimental and simulated Bode plots for the impedance experiments reported in Figure 3. Operating conditions: LSCF-GDC/GDC/LSCF-GDC symmetric cell, open circuit voltage, 10 mV, 10 kHz – 10 mHz, T = 560°C – 700°C, P O_2 = 5% – 21%.

Figure 5 – A) Effect of O_2 dilution at 700°C and OCV. Comparison between impedance spectra measured with 5% O_2 diluted in N_2 (green symbols) and in He (orange symbols). B) Arrhenius plots of the ohmic resistance (●) and of the polarization resistance (■). C) Simulated spectra at 5% O_2. Orange line is the simulation performed with He to balance and without the CSTR boundary condition.

Green line is simulation performed with N_2 to balance and with the CSTR boundary condition.

Figure 6 – Model analysis of the experimental impedance spectra measured by Nielsen et al. [6] on LSCF-GDC/GDC/LSCF-GDC symmetric cells. The data set refers to the moderately coarse sample. The experiments are performed in air at OCV. The original spectra are normalized by removal of the ohmic resistance associated to the GDC electrolyte.

Figure 7 – Sensitivity analysis on the input model parameters. The sensitivity parameter SP (inset) is calculated with 10% variation of each parameter ($\Delta k/k = \pm 0.1$). The operating conditions refer to experiments in air and OCV at varying temperature from 560°C to 700°C. Full bars refer to +10% variation, dashed bars to -10% variation.

Figure 8 – Variation of the simulated polarization resistance as a function of electrode thickness and current density: (—) OCV, (—) 0.5 A/m^2, (—) 1 A/m^2. Point A: 10 µm thickness. Point B: 6 µm thickness. Point C: 100 µm thickness. Inserts show the impedance spectra simulated in correspondence of the highlighted points.

Figure 9 – Evolution of the ionic and electronic current density along the axis of the composite electrode as simulated by the model under the conditions highlighted in the three points of Figure 8. Black line (—) is electronic current, red line (—) is ionic current flowing in GDC, green line (—) is ionic current flowing in LSCF.

Nomenclature

A = thermodynamic factor [-]

a_v^{ads} = surface to volume ratio [m^2 m^{-3}]

a_v^{int} = interfacial surface to volume ratio [m^2 m^{-3}]

$\hat{a}_{V_{ö,M}}$ = activity of the oxygen vacancies

C_{DL}^{int} = cathode/electrolyte interfacial double layer capacitance [F m^{-2}]

C_{DL}^{surf} = surface capacitance [F m^{-2}]

C_{O_2} = concentration of molecular O_2 [mol m^{-3}]

C_{mc} = maximum stoichiometric concentration of oxide ions in the lattice [mol m^{-3}]

$C_{V_{ö}}$ = concentration of oxygen vacancies [mol m^{-3}]

$C_{O_ö^x}$ = concentration of oxide ion in the lattice [mol m^{-3}]

d_p = particle size [μm]

$D_{V_{ö,M}}$ = diffusion of the oxygen vacancies [m^2 s^{-1}]

D_{O_2,N_2}^{Mol} = molecular binary diffusion of O_2 in N_2 [m^2 s^{-1}]

$D_{O_2}^{Knu}$ = Knudsen diffusion of O_2 [m^2 s^{-1}]

E_{Act} = activation energy [J mol^{-1}]

F = Faraday constant [C mol^{-1}]

F^{In} = inlet molar flow rate [mol s^{-1}]

F^{Out} = outlet molar flow rate [mol s^{-1}]

f_E = volume fraction of electrolyte particles in a binary mixture [-]

f_M = volume fraction of MIEC particles in a binary mixture [-]

H_i = specific molar enthalpy of the ith species [J/mol]

$\hat{I}_{tot}$ = total current density [A cm^{-2}]

J_i = molar flow of the ith species [mol m^{-2} s^{-1}]

j = imaginary unit

k = pre-exponential factors of the kinetic rate

L = electrode thickness [m]

n_{e-} = number of electrons exchanged in the charge transfer reactions

P_{O_2} = partial pressure of O_2 [Pa]

R = gas constant [J mol^{-1} K^{-1}]

r_j = rate of the jth reaction [mol m^{-2} s^{-1}]

S_{eld} = geometrical surface of the electrode [m^2]

S_i = specific entropy of the ith species [J/mol/K]

T = temperature [K]

t = time [s]

V_{eld} = electrode voltage [V]

y_{O_2} = O_2 molar fraction

Z = impedance [Ω cm^2]

$Z_{E,E}$ = contact number between electrolyte particles in the binary mixture [-]

$Z_{M,M}$ = contact number between electrolyte particles in the binary mixture [-]

z = axial coordinate [m]

Greek Symbols

α = charge transfer coefficient

γ = constant phase element exponent [-]

Γ = surface site concentration [mol m^{-2}]

δ = oxygen stoichiometry parameter in LSCF

ε = electrode porosity

η = bulk overpotential [V]

θ_F = surface coverage of the free sites

θ_i = surface coverage of the ith species

λ_{TPB} = specific length per unit volume of the three phase boundary [m m^{-3}]

σ = conductivity [S m^{-1}]

τ = electrode tortuosity

ϕ = potential [V]

χ = surface potential [V]

ω = frequency [s^{-1}]

Subscripts and superscripts

0 = referred to the inlet boundary condition (current collector/electrode interface)

~ = perturbed variable

b = referred to the bulk

E = referred to the electrolyte

eff = effective

ele = electronic

eld = electrode

ely = electrolyte

End = referred to the outlet boundary condition (electrolyte/electrode interface)

eq = equilibrium

i = ith species

ion = ionic

j = jth species

M = referred to the MIEC

max = maximum

min = minimum

s = referred to the surface

ss = steady-state

Species

O_2 = molecular oxygen

O_M^{ads} = oxygen atom adsorbed on the MIEC surface

O_M^{-ads} = charged oxygen atom adsorbed on the MIEC surface

$V_{\ddot{o},M}$ = oxide ion vacancy in the MIEC lattice

$O_{o,M}^{x}$ = oxide ion in the MIEC lattice

$V_{\ddot{o},E}$ = oxide ion vacancy in the electrolyte lattice

$O_{o,E}^{x}$ = oxide ion in the electrolyte lattice

$ = free surface site

References

[1] F.S. Baumann, J. Fleig, H.-U. Habermeier, J. Maier, Impedance spectroscopic study on well-defined (La,Sr)(Co,Fe)O3−δ model electrodes, Solid State Ionics, 177 (2006) 1071-1081.

[2] W.C. Chueh, S.M. Haile, Electrochemistry of Mixed Oxygen Ion and Electron Conducting Electrodes in Solid Electrolyte Cells, Annual Review of Chemical and Biomolecular Engineering, 3 (2012) 313-341.

[3] A. Esquirol, N.P. Brandon, J.A. Kilner, M. Mogensen, Electrochemical Characterization of La0.6Sr0.4Co0.2Fe0.8 O 3 Cathodes for Intermediate-Temperature SOFCs, Journal of The Electrochemical Society, 151 (2004) A1847-A1855.

[4] H. Wang, K.J. Yakal-Kremski, T. Yeh, G.M. Rupp, A. Limbeck, J. Fleig, S.A. Barnett, Mechanisms of Performance Degradation of (La,Sr)(Co,Fe)O3-δ Solid Oxide Fuel Cell Cathodes, Journal of The Electrochemical Society, 163 (2016) F581-F585.

[5] E. Perry Murray, M.J. Sever, S.A. Barnett, Electrochemical performance of (La,Sr)(Co,Fe)O3–(Ce,Gd)O3 composite cathodes, Solid State Ionics, 148 (2002) 27-34.

[6] J. Nielsen, T. Jacobsen, M. Wandel, Impedance of porous IT-SOFC LSCF:CGO composite cathodes, Electrochimica Acta, 56 (2011) 7963-7974.

[7] N. Grunbaum, L. Dessemond, J. Fouletier, F. Prado, L. Mogni, A. Caneiro, Rate limiting steps of the porous La0.6Sr0.4Co0.8Fe0.2O3−δ electrode material, Solid State Ionics, 180 (2009) 1448-1452.

[8] M. Prestat, A. Infortuna, S. Korrodi, S. Rey-Mermet, P. Muralt, L.J. Gauckler, Oxygen reduction at thin dense La0.52Sr0.48Co0.18Fe0.82O3–δelectrodes, Journal of Electroceramics, 18 (2007) 111-120.

[9] Y.T. Kim, N. Shikazono, Investigation of La0.6Sr0.4CoO3−δ-Gd0.1Ce0.9O2−δ composite cathodes with different volume ratios by three dimensional reconstruction, Solid State Ionics, 309 (2017) 77-85.

[10] V. Yurkiv, R. Costa, Z. Ilhan, A. Ansar, W.G. Bessler, Impedance of the Surface Double Layer of LSCF/CGO Composite Cathodes: An Elementary Kinetic Model, Journal of The Electrochemical Society, 161 (2014) F480-F492.

[11] F. Qiang, K. Sun, N. Zhang, X. Zhu, S. Le, D. Zhou, Characterization of electrical properties of GDC doped A-site deficient LSCF based composite cathode using impedance spectroscopy, Journal of Power Sources, 168 (2007) 338-345.

[12] C. Endler-Schuck, J. Joos, C. Niedrig, A. Weber, E. Ivers-Tiffée, The chemical oxygen surface exchange and bulk diffusion coefficient determined by impedance spectroscopy of porous La0.58Sr0.4Co0.2Fe0.8O3−δ (LSCF) cathodes, Solid State Ionics, 269 (2015) 67-79.

[13] Y.-M. Kim, S.-I. Pyun, J.-S. Kim, G.-J. Lee, Mixed Diffusion and Charge-Transfer-Controlled Oxygen Reduction on Dense La1 − x Sr x Co0.2Fe0.8O3 − δ Electrodes with Various Sr Contents, Journal of The Electrochemical Society, 154 (2007) B802-B809.

[14] J. Laurencin, M. Hubert, K. Couturier, T.L. Bihan, P. Cloetens, F. Lefebvre-Joud, E. Siebert, Reactive Mechanisms of LSCF Single-Phase and LSCF-CGO Composite Electrodes Operated in Anodic and Cathodic Polarisations, Electrochimica Acta, 174 (2015) 1299-1316.

[15] M. Prestat, J.-F. Koenig, L.J. Gauckler, Oxygen reduction at thin dense La0.52Sr0.48Co0.18Fe0.82O3–δelectrodes, Journal of Electroceramics, 18 (2007) 87-101.

[16] C.R. Kreller, M.E. Drake, S. Adler, Influence of Electrode Morphology on Electrochemical Response of SOFC Cathodes, ECS Transactions, 28 (2010) 105-121.

[17] W.G. Wang, M. Mogensen, High-performance lanthanum-ferrite-based cathode for SOFC, Solid State Ionics, 176 (2005) 457-462.

[18] J. Nielsen, J. Hjelm, Impedance of SOFC electrodes: A review and a comprehensive case study on the impedance of LSM:YSZ cathodes, Electrochimica Acta, 115 (2014) 31-45.

[19] Y.T. Kim, Z. Jiao, N. Shikazono, Evaluation of La0.6Sr0.4Co0.2Fe0.8O3-Gd0.1Ce0.9O1.95 composite cathode with three dimensional microstructure reconstruction, Journal of Power Sources, 342 (2017) 787-795.

[20] K. Matsuzaki, N. Shikazono, N. Kasagi, Three-dimensional numerical analysis of mixed ionic and electronic conducting cathode reconstructed by focused ion beam scanning electron microscope, Journal of Power Sources, 196 (2011) 3073-3082.

[21] A. Häffelin, J. Joos, M. Ender, A. Weber, E. Ivers-Tiffée, Time-Dependent 3D Impedance Model of Mixed-Conducting Solid Oxide Fuel Cell Cathodes, Journal of The Electrochemical Society, 160 (2013) F867-F876.

[22] X.J. Chen, S.H. Chan, K.A. Khor, Simulation of a composite cathode in solid oxide fuel cells, Electrochimica Acta, 49 (2004) 1851-1861.

[23] A. Bertei, M.P. Carpanese, D. Clematis, A. Barbucci, M.Z. Bazant, C. Nicolella, Understanding the electrochemical behaviour of LSM-based SOFC cathodes. Part II - Mechanistic modelling and physically-based interpretation, Solid State Ionics, 303 (2017) 181-190.

[24] M.P. Carpanese, D. Clematis, A. Bertei, A. Giuliano, A. Sanson, E. Mercadelli, C. Nicolella, A. Barbucci, Understanding the electrochemical behaviour of LSM-based SOFC cathodes. Part I — Experimental and electrochemical, Solid State Ionics, 301 (2017) 106-115.

[25] Y. Fu, S. Poizeau, A. Bertei, C. Qi, A. Mohanram, J.D. Pietras, M.Z. Bazant, Heterogeneous electrocatalysis in porous cathodes of solid oxide fuel cells, Electrochimica Acta, 159 (2015) 71-80.

[26] A. Donazzi, M. Maestri, G. Groppi, A multistep model for the kinetic analysis of the impedance spectra of a novel mixed ionic and electronic conducting cathode, Electrochimica Acta, 222 (2016) 1029-1044.

[27] A. Banerjee, O. Deutschmann, Elementary kinetics of the oxygen reduction reaction on LSM-YSZ composite cathodes, Journal of Catalysis, 346 (2017) 30-49.

[28] S.B. Adler, J.A. Lane, B.C.H. Steele, Electrode Kinetics of Porous Mixed□ Conducting Oxygen Electrodes, Journal of The Electrochemical Society, 143 (1996) 3554-3564.

[29] S.B. Adler, Mechanism and kinetics of oxygen reduction on porous La1−xSrxCoO3−δ electrodes, Solid State Ionics, 111 (1998) 125-134.

[30] A. Lasia, Modeling of Impedance of Porous Electrodes, in: M. Schlesinger (Ed.) Modeling and Numerical Simulations, Springer New York, New York, NY, 2009, pp. 67-137.

[31] J.E. Mortensen, M. Søgaard, T. Jacobsen, Analytical, 1-Dimensional Impedance Model of a Composite Solid Oxide Fuel Cell Cathode, Journal of The Electrochemical Society, 161 (2014) F161-F175.

[32] J.E. Mortensen, M. Sø/gaard, T. Jacobsen, Impedance Modeling of Solid Oxide Fuel Cell Cathodes, ECS Transactions, 28 (2010) 17-38.

[33] E. Effori, H. Moussaoui, F. Monaco, R.K. Sharma, J. Debayle, Y. Gavet, G. Delette, G. Si Larbi, E. Siebert, J. Vulliet, L. Dessemond, J. Laurencin, Reaction Mechanism and Impact of Microstructure on Performances for the LSCF-CGO Composite Electrode in Solid Oxide Cells, Fuel Cells, 19 (2019) 429-444.

[34] V.M. Janardhanan, O. Deutschmann, Modeling diffusion limitation in solid-oxide fuel cells, Electrochimica Acta, 56 (2011) 9775-9782.

[35] M. Rahmanipour, A. Pappacena, M. Boaro, A. Donazzi, A Distributed Charge Transfer Model for IT-SOFCs Based on Ceria Electrolytes, Journal of The Electrochemical Society, 164 (2017) F1249-F1264.

[36] J. Fleig, On the current–voltage characteristics of charge transfer reactions at mixed conducting electrodes on solid electrolytes, Physical Chemistry Chemical Physics, 7 (2005) 2027-2037.

[37] J. Fleig, Solid Oxide Fuel Cell Cathodes: Polarization Mechanisms and Modeling of the Electrochemical Performance, Annual Review of Materials Research, 33 (2003) 361-382.

[38] H. Zhang, M. Gong, K. Gerdes, X. Liu, Surface Transport Mechanism and Bi-Pathway ORR Kinetics for Solid Oxide Fuel Cell Cathode, Journal of The Electrochemical Society, 161 (2014) F983-F990.

[39] M. Gong, R.S. Gemmen, D.S. Mebane, K. Gerdes, X. Liu, Simulation of Surface-Potential Driven ORR Kinetics on SOFC Cathode with Parallel Reaction Pathways, Journal of The Electrochemical Society, 161 (2014) F344-F353.

[40] D.S. Mebane, M. Liu, Classical, phenomenological analysis of the kinetics of reactions at the gas-exposed surface of mixed ionic electronic conductors, Journal of Solid State Electrochemistry, 10 (2006) 575-580.

[41] W.G. Bessler, S. Gewies, M. Vogler, A new framework for physically based modeling of solid oxide fuel cells, Electrochimica Acta, 53 (2007) 1782-1800.

[42] X. Jin, R.E. White, K. Huang, Simulating Charge Transport in Solid Oxide Mixed Ionic and Electronic Conductors: Nernst-Planck Theory vs Modified Fick's Law, Journal of The Electrochemical Society, 163 (2016) A2702-A2719.

[43] A. Bertei, G. Arcolini, J.P. Ouweltjes, Z. Wuillemin, P. Piccardo, C. Nicolella, PHYSICALLY-BASED DECONVOLUTION OF IMPEDANCE SPECTRA: INTERPRETATION, FITTING AND VALIDATION OF A NUMERICAL MODEL FOR LANTHANUM STRONTIUM COBALT FERRITE-BASED SOLID OXIDE FUEL CELLS, Electrochimica Acta, 208 (2016) 129-141.

[44] A. Bertei, J. Mertens, C. Nicolella, Electrochemical Simulation of Planar Solid Oxide Fuel Cells with Detailed Microstructural Modeling, Electrochimica Acta, 146 (2014) 151-163.

[45] P. Costamagna, P. Costa, V. Antonucci, Micro-modelling of solid oxide fuel cell electrodes, Electrochimica Acta, 43 (1998) 375-394.

[46] J.H. Nam, D.H. Jeon, A comprehensive micro-scale model for transport and reaction in intermediate temperature solid oxide fuel cells, Electrochimica Acta, 51 (2006) 3446-3460.

[47] D. Chen, Z. Lin, H. Zhu, R.J. Kee, Percolation theory to predict effective properties of solid oxide fuel-cell composite electrodes, Journal of Power Sources, 191 (2009) 240-252.

[48] W. Lai, F. Ciucci, Mathematical modeling of porous battery electrodes—Revisit of Newman's model, Electrochimica Acta, 56 (2011) 4369-4377.

[49] J.S. Newman, K.E. Thomas-Alyea, Electrochemical systems, John Wiley & Sons, Ltd, Hoboken, New Jersey, 2004.

[50] M. Maestri, K. Reuter, Semiempirical Rate Constants for Complex Chemical Kinetics: First-Principles Assessment and Rational Refinement, Angewandte Chemie International Edition, 50 (2011) 1194-1197.

[51] A.B. Mhadeshwar, H. Wang, D.G. Vlachos, Thermodynamic Consistency in Microkinetic Development of Surface Reaction Mechanisms, The Journal of Physical Chemistry B, 107 (2003) 12721-12733.

[52] K.E. Starling, The properties of gases and liquids, Third Edition, Robert C. Reid, John M. Prausnitz and Thomas K. Sherwood, McGraw-Hill (1977), 688 pages, $27.50, AIChE Journal, 24 (1978) 1142-1142.

[53] S.R. Bishop, K.L. Duncan, E.D. Wachsman, Surface and Bulk Defect Equilibria in Strontium-Doped Lanthanum Cobalt Iron Oxide, Journal of The Electrochemical Society, 156 (2009) B1242-B1248.

[54] S. Wang, H. Inaba, H. Tagawa, M. Dokiya, T. Hashimoto, Nonstoichiometry of Ce0.9Gd0.1O1.95−x, Solid State Ionics, 107 (1998) 73-79.

[55] M. Mogensen, N.M. Sammes, G.A. Tompsett, Physical, chemical and electrochemical properties of pure and doped ceria, Solid State Ionics, 129 (2000) 63-94.

[56] S.R. Bishop, K.L. Duncan, E.D. Wachsman, Surface and bulk oxygen non-stoichiometry and bulk chemical expansion in gadolinium-doped cerium oxide, Acta Materialia, 57 (2009) 3596-3605.

[57] Y. Choi, M.C. Lin, M. Liu, Rational design of novel cathode materials in solid oxide fuel cells using first-principles simulations, Journal of Power Sources, 195 (2010) 1441-1445.

[58] H.J.M. Bouwmeester, M.W. Den Otter, B.A. Boukamp, Oxygen transport in La0.6Sr0.4Co1−yFeyO3−δ, Journal of Solid State Electrochemistry, 8 (2004) 599-605.

[59] A. He, Y. Kim, N. Shikazono, Numerical Simulation of LSCF-GDC Composite Cathodes with Various Microstructures, ECS Transactions, 78 (2017) 2751-2763.

[60] A. He, T. Shimura, J. Gong, N. Shikazono, Numerical simulation of La0.6Sr0.4Co0.2Fe0.8O3- Gd0.1Ce0.9O1.95 composite cathodes with micro pillars, International Journal of Hydrogen Energy, 44 (2019) 6871-6885.

[61] M.G.H.M. Hendriks, J.E. ten Elshof, H.J.M. Bouwmeester, H. Verweij, The electrochemical double-layer capacitance of yttria-stabilised zirconia, Solid State Ionics, 146 (2002) 211-217.

[62] M. Orazem, B. Tribollet, Electrochemical Impedance Spectroscopy, John Wiley & Sons, Hoboken, New Jersey, 2008.

[63] S. Campanella, M. Bracconi, A. Donazzi, A fast regression model for the interpretation of electrochemical impedance spectra of Intermediate Temperature Solid Oxide Fuel Cells, Journal of Electroanalytical Chemistry, 823 (2018) 697-712.

[64] B.C.H. Steele, Appraisal of Ce1−yGdyO2−y/2 electrolytes for IT-SOFC operation at 500°C, Solid State Ionics, 129 (2000) 95-110.

[65] A. Bertei, C. Nicolella, A comparative study and an extended theory of percolation for random packings of rigid spheres, Powder Technology, 213 (2011) 100-108.

[66] J.W. Stevenson, T.R. Armstrong, R.D. Carneim, L.R. Pederson, W.J. Weber, Electrochemical Properties of Mixed Conducting Perovskites La1 − x M x Co1 − y Fe y O 3 − δ (M = Sr, Ba, Ca), Journal of The Electrochemical Society, 143 (1996) 2722-2729.

[67] A. Bertei, A. Barbucci, M.P. Carpanese, M. Viviani, C. Nicolella, Morphological and electrochemical modeling of SOFC composite cathodes with distributed porosity, Chemical Engineering Journal, 207-208 (2012) 167-174.

[68] A. Barbucci, M. Paola Carpanese, M. Viviani, N. Vatistas, C. Nicolella, Morphology and electrochemical activity of SOFC composite cathodes: I. experimental analysis, Journal of Applied Electrochemistry, 39 (2009) 513-521.

[69] G.W. Coffey, L.R. Pederson, P.C. Rieke, Competition Between Bulk and Surface Pathways in Mixed Ionic Electronic Conducting Oxygen Electrodes, Journal of The Electrochemical Society, 150 (2003) A1139-A1151.

- A dynamic heterogenous and physic model of composite LSCF-GDC cathodes is presented
- Electrochemical impedance spectra are simulated with a detailed kinetic ORR scheme
- Consistent rate parameters are derived by fitting to experimental spectra
- Simultaneous oxide ion flow in LSCF and GDC occurs at high applied current density
- The transfer of a single-charged oxygen adatom from LSCF to GDC is the RDS

Author statement

Alessandro Donazzi: Conceptualization, Methodology, Software, Writing - Original Draft.

Giulio Cordaro: Investigation, Validation, Resources

Andrea Baricci: Conceptualization, Writing - Review & Editing

Zhao-Bin Ding: Software, Formal analysis

Matteo Maestri: Conceptualization, Writing - Review & Editing.

Declaration of interests

☒ The authors declare that they have no known competing financial interests or personal relationships that could have appeared to influence the work reported in this paper.

☐The authors declare the following financial interests/personal relationships which may be considered as potential competing interests: